Journal of Wind Engineering & Industrial Aerodynamics 197 (2020) 104058

Contents lists available at ScienceDirect

Journal of Wind Engineering & Industrial Aerodynamics

journal homepage: www.elsevier.com/locate/jweia

Aerodynamic shape optimization of barriers for windblown sand mitigation using CFD analysis

Marko Horvat [a,*], Luca Bruno [a,c], Sami Khris [b,c], Lorenzo Raffaele [a,c]

[a] Politecnico di Torino, Department of Architecture and Design, Viale Mattioli 39, I-10125, Torino, Italy
[b] Optiflow Company, 160, Chemin de la Madrague-Ville, F-13015, Marseille, France
[c] Windblown Sand Modelling and Mitigation Joint Research Group, Italy

ARTICLE INFO

Keywords:
windblown sand
Sand mitigation measures
Aerodynamic optimization
Computational fluid dynamics

ABSTRACT

Protection from windblown sand is one of the key engineering issues for construction and maintenance of human infrastructures in arid environments. In the last decades, a number of barrier-type Sand Mitigation Measures with different shapes have been proposed in order to overcome this problem. Sand barriers are often deployed alongside long line-like infrastructures crossing vast desert regions. It follows that highly optimized preliminary design of the barrier cross section is of paramount importance in the perspective of a large-scale production, in order to minimize the construction costs per unit length, and maximize the aerodynamic performances. The present computational study aims to adapt and apply aerodynamic optimization to a windblown sand barrier. The search for the optimum is carried out on Computational Fluid Dynamics simulations, without recourse to surrogate models. Both gradient-based method and genetic algorithm are used, in the light of the features of the goal function previously sampled by extensive sensitivity studies. The approach is applied to two constructive forms of the same barrier having increasing complexity. Results are critically discussed by combining complementary remarks on the optimization convergence, the phenomenological reading of the flow around the optimized barrier, and its design and construction.

1. Introduction

Wind engineering is currently increasingly called upon to investigate windblown sand. In fact, windblown sand harmfully interacts with various civil structures and infrastructures in arid and desert environments (Middleton and Sternberg, 2013): pipelines (Kerr and Nigra, 1952), industrial facilities (Alghamdi and Al-Kahtani, 2005), towns (Zhang et al., 2007), single buildings (Rizvi, 1989; Bofah and Al-Hinai, 1986), farms (Wang et al., 2010), roads (Redding and Lord, 1981), and railways (Bruno et al., 2018c).

Since the pioneering researches of Bagnold (1936, 1937, 1941), O'Brien and Rindlaub (1936), Chepil (1945) and Kawamura (1951) up to the recent and comprehensive monographs by Shao (2008), Zheng (2009) and Pye and Tsoar (2009), a duly attention was paid by researchers to observing, understanding and modelling the fundamental phenomena of erosion, transport, sedimentation (Preziosi et al., 2015) and avalanching (Lo Giudice et al., 2018) of the sand induced by the wind.

Concomitantly, attempts were made to design measures able to protect infrastructures from windblown sand (*Sand Mitigation Measures*, SMMs), in a genuine problem-solving perspective driven by real world technical problems. Among early proposals of SMMs, let us recall the pioneering patented solution of Pettus Newell (1903), the ones empirically tested along the Kundian-Mianwali section of the Sher Shah-Attock railway in the arid Punjab province of Pakistan (probably built in 1891, surely in service in 1910, Rahim, 1945), the ones conceived by J.H. Gildea along the Dammam-Riyadh railway in Kingdom of Saudi Arabia (1947–1950 Henry, 1952), the ones deployed along the Batou-Lanzhou railway across the Tengger Desert in China (built in 1956, Mitchell et al., 1996). In order to sort out the broad panoply of SMMs proposed in the last decades, the recent state-of-art review by Bruno et al. (2018c) collects and categorizes both windblown sand-induced performance deficiencies of the infrastructures (windblown Sand Ultimate Limit States and Serviceability Limit States) and the prevention techniques to mitigate the windblown sand effects (Source-Path-Receiver categorization of the Sand Mitigation Measures, Fig. 1).

* Corresponding author.
E-mail address: marko.horvat@polito.it (M. Horvat).
URL: http://www.smart-eid.eu (M. Horvat).

https://doi.org/10.1016/j.jweia.2019.104058
Received 29 March 2019; Received in revised form 6 September 2019; Accepted 3 December 2019
Available online xxxx

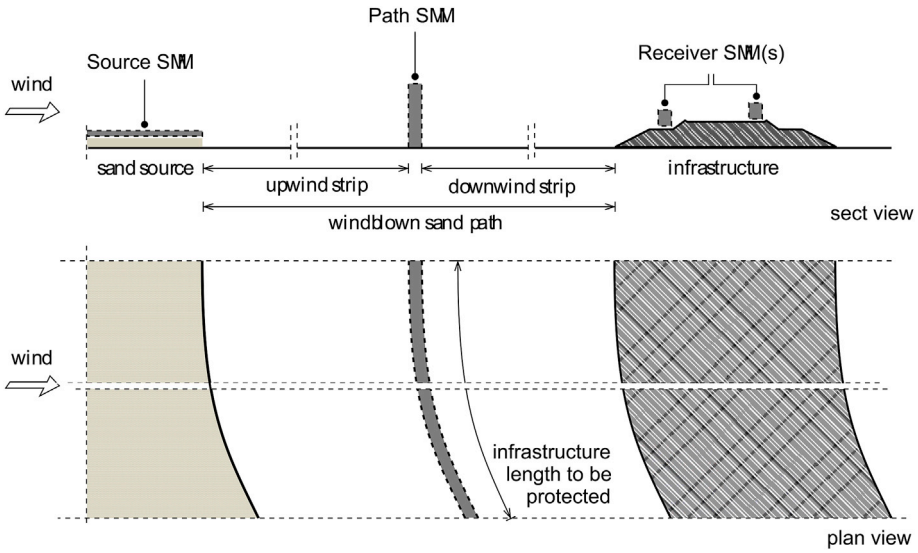

Fig. 1. Conceptual scheme of the Sand, Path and Receiver SMMs: cross section and plan view.

Source SMMs are directly located over the sand source surface (dunes or loose sand sheets): although they are widely adopted against desertification process at regional scales, they are beyond the field of interest, the role, and the economic capabilities of infrastructures owners, designers, and general contractors. *Receiver* SMMs are directly located on the infrastructure and addressed to protect its single components: as a result, they strongly depend on the type of the infrastructure to be protected. *Path* SMMs are located along the infrastructure, and across the windblown sand path from the sand source to the infrastructure. They are generally intended to modify the wind flow, to trap windblown sand, and to protect the whole infrastructure. Path-type SMMs include surface-like SMMs (porous fences, solid barriers) and volume-like SMMs (berms and ditches), or their combinations.

In the light of the categorization above, we believe the design of SMMs in general, and of Path SMMs in particular, should satisfy two main methodological requirements. First, Path SMMs need the most of all a rational aerodynamic conceptual design, grounded on the clear phenomenological setting of their aerodynamic working principles, and the quantitative assessment of the wind flow around them. Second, Path SMMs are often deployed alongside long line-like infrastructures (e.g. railways, roads and highways, pipelines) crossing vast desert regions. In such cases, the infrastructure length to be protected is often dozen- or hundred-kilometer long (Fig. 1). It follows that highly optimized preliminary design of the Path SMM cross section is recommended in the perspective of a large-scale production, in order to minimize the construction costs per unit length and maximize the aerodynamic performances.

Aerodynamic conceptual design of Path SMMs was mainly handled in the past by a trial-and-error approach based upon installation and field trials (Li and Sherman, 2015). In a recent computational study, Bruno et al. (2018b) contribute to systematically and quantitatively clarifying the working principles of different SMMs, define their sand trapping performance metrics, relate them to some key geometrical features of the SMMs, and propose general design guidelines.

Aerodynamic optimization has attracted the growing attention of the scientific community over the past 60 years. Thanks to this research activity, several automated design optimization procedures and algorithms are available nowadays, recently reviewed by Skinner and Zare-Behtash (2018). Thanks to continuous advancements in computational resources, optimization has now become a key-component for aerodynamic design, with applications to many industrial fields, e.g. aerospace (since Hicks et al., 1974), turbomachinery (reviewed by Li and Zheng, 2017), automotive (e.g. Dumas, 2008) and train aerodynamics (e.g. Munoz-Paniagua and Garcia, 2019), energy harvesting, internal pipe and cavity flows, among others. Applications to the field of wind/structural engineering suffer a relative delay, mainly induced by the high cost of the computational simulation of the turbulent, high-Reynolds wind flow around bluff bodies (Asghari Mooneghi and Kargarmoakhar, 2016), by the simulation of the Atmospheric Boundary Layer (ABL, Bernardini et al., 2015), and by the specific features of each single project, that make difficult the large-scale production and hardly justify the optimization. Aerodynamic optimization was early applied to general trapezoidal bluff cylinders by Burman et al. (2002) and Mack et al. (2005), while a recent application to circular cylinders can be found in Karthik et al. (2018). Perspective applications to specific civil structures include building aerodynamics (Bobby et al., 2013; Bernardini et al., 2015; Elshaer et al., 2015, 2017; Ding and Kareem, 2018), and bridge deck aerodynamics (Cid Montoya et al., 2018b, a).

In the light of the current needs, limitations and opportunities outlined above, the present study aims at adapting and applying aerodynamic optimization procedure to a Path Sand Mitigation Measure, namely the solid barrier proposed by Bruno et al. (2016) and studied in Bruno et al. (2018b).

The paper is organized in five further sections. Section 2 summarizes the wind flow modeling and computational approach adopted. In Section 3, the used optimization approaches are briefly recalled and discussed with respect to the current state-of-art in wind engineering optimization. The solid barrier selected as baseline solution is described in Section 4, together with the outline of the optimization setup. The findings of the preliminary parametrical study and the optimization results are critically discussed in Sections 5 and 6, respectively. Finally, conclusions and perspectives are outlined in Section 7.

2. Wind flow modeling and computational approach

In a general modelling perspective, windblown sand phenomena should be simulated by accounting for both wind and sand flow. In an engineering perspective, at the detailed design stage the accurate barrier performance shall be assessed by means of physical tests, i.e. full-scale field tests in windy and sandy environments or by scaled wind tunnel tests with incoming drifting sand (e.g. Bruno et al., 2018a). Alternatively, its performance can be assessed by means of multiphase Computational Fluid Dynamics simulations (e.g. Preziosi et al., 2015; Lo Giudice et al., 2018) by adopting time evolving free sand-surface boundary conditions. Both wind tunnel tests and multiphase simulations are not affordable within the preliminary design phase and related optimization studies

because of their high cost. At this stage, the SMM performances can be estimated by means of purely aerodynamic metrics defining the region where the local wind flow induces sand accumulation, as defined in Bruno et al. (2018b). Indeed, the SMMs have maximum sand trapping performances without sedimented sand around them, and sand sedimentation involves the monotonic decrease of their performances (see Bruno et al., 2018a). Hence, purely wind simulations are able to estimate the maximum SMM performance. Moreover, even if purely aerodynamic metrics are expected to be approximated, they are able to describe the relative performances of different alternative solutions, as demonstrated in Bruno et al. (2018b). In the light of the above, in the present study single fluid phase simulations are carried out.

Most of the studies cited in Section 1 adopt two-dimensional (2D) computational domains that refer to horizontal planes far from the ground level for applications to high rise buildings, or to vertical planes around bridge decks far from the ground surface. Consistently with the assumption above, in such studies uniform incoming wind is adopted at inlet boundary: in other terms, the ABL is not accounted for during optimization. Conversely, in this study the 2D domain includes ABL having in mind that the SMMs are low rise structures mounted on the ground surface.

In the same computational cost-saving perspective, most of the studies cited in Section 1 adopt Reynolds Average Navies-Stokes (RANS) approach to turbulence modeling. Higher fidelity models (Large Eddy Simulations, LES) are only partially adopted by Ding and Kareem (2018) and in full by Elshaer et al. (2017), when the minimization of the fluctuating wind forces is the optimization goal, or one of the objectives. In this study, a steady RANS approach is adopted having in mind that: (i) unsteady fluid phenomena can be neglected to the aims of the assessment of aerodynamic performances of the barrier since sand mass transport happens at a much larger time scale than turbulence characteristic time scales; (ii) reference is made to equivalent static wind force corresponding to the extreme effect of the turbulent wind to assess the cost of the barrier in the preliminary design stage. In particular, the SST $k-\omega$ turbulence model is selected for the current application because of its proven accuracy in bluff body aerodynamics in general (Menter et al., 2003). The whole adopted computational model described below has been validated against accurate wind tunnel tests in Bruno and Fransos (2015) for the same class of aerodynamic problems, i.e. a nominal 2D bluff body immersed in a turbulent ABL. The same computational model has been adopted to study the aerodynamic behavior of windblown sand solid barriers in Bruno et al. (2018b). Additionally, Reynolds Averaged approach has been widely used for comparable configurations in dune aerodynamics analysis (e.g. in Liu et al., 2011; Araújo et al., 2013; Bruno and Fransos, 2015; Lima et al., 2017). The adapted Navier-Stokes equations (Eq. (1) and Eq. (2)) with the SST $k-\omega$ turbulence model (Eq. (3) and Eq. (4)) read (Menter, 1994; Menter et al., 2003):

$$\frac{\partial \overline{u}_i}{\partial x_i} = 0 \,, \tag{1}$$

$$\overline{u}_j \frac{\partial \overline{u}_i}{\partial x_i} = -\frac{1}{\rho}\frac{\partial \overline{p}}{\partial x_i} + \left[\nu\left(\frac{\partial \overline{u}_i}{\partial x_j} + \frac{\partial \overline{u}_j}{\partial x_i}\right)\right] - \frac{\partial}{\partial x_j}\left(\overline{u'_i u'_j}\right) \,, \tag{2}$$

$$\overline{u}_j \frac{\partial k}{\partial x_i} = \frac{\partial}{\partial x_i}\left[\left(\sigma_k \nu_t + \nu\right)\frac{\partial k}{\partial x_i}\right] + \tilde{P}_k - \beta^* k\omega \tag{3}$$

$$\overline{u}_j \frac{\partial \omega}{\partial x_i} = \frac{\partial}{\partial x_i}\left[\left(\sigma_\omega \nu_t + \nu\right)\frac{\partial \omega}{\partial x_i}\right] + \alpha\frac{\omega}{k}P_k - \beta\omega^2 + (1-F_1)\frac{2\sigma_\omega}{\omega}\frac{\partial k}{\partial x_i}\frac{\partial \omega}{\partial x_i}. \tag{4}$$

In the previous equations $\overline{u}_i$ is the averaged velocity, u' the velocity fluctuating component, $\overline{p}$ the averaged pressure, ρ the air density, ν the air kinematic viscosity, k is the turbulent kinetic energy, ω its specific dissipation rate and ν_t the so-called turbulent kinematic viscosity. The kinetic energy production term $\tilde{P}_k$ is modeled by introducing a production limiter to prevent the build-up of turbulence in stagnation regions:

$$\tilde{P}_k = \min(P_k, 10\beta^* k\omega) \quad \text{where} \quad P_k \approx 2\nu_t D_{ij}\frac{\partial \overline{u}_i}{\partial x_i}.$$

For the sake of conciseness, the definition of the blending function F_1 and the values of the model constants are omitted herein. Interested readers can find them in Menter et al. (2003). To model the near wall region, the wall function approach is used. Briefly, this means: i. for k, zero-gradient Neumann boundary condition is used; ii. for ω, a Dirichlet boundary condition is used, calculated from the blending of viscous and logarithmic component; iii. for ν_t, Dirichlet boundary condition is obtained from k.

The adopted 2D computational domain is shown in Fig. 2. The computational domain includes the flat ground both upwind and downwind the barrier, and the barrier itself. We indicate as far-field all the quantities incoming, with the aim to model the environmental conditions around the computational domain. The upwind far-field is modeled by means of inlet boundary conditions: a Neumann condition is used for pressure, while Dirichlet conditions are imposed on u, k and ω. The far-field incoming wind velocity profile is prescribed using the log-law $u(z) = \frac{u^*}{k}\log\left(\frac{z+z_0}{z_0}\right)$, where $k = 0.41$ is the von Karman constant, u_* is the friction velocity, z_0 is the aerodynamic roughness. The profiles of $k(z)$ and $\omega(z)$ are set in accordance to Richards and Norris (2011) to replicate the atmospheric wind flow. At outlet, for all the flow parameters zero-gradient condition is imposed. No-slip conditions are imposed at the ground surface and at barrier wall.

The space discretization is accomplished by a completely structured grid consisting of hexahedral cells. The mesh is refined along the ground and at the barrier walls, so that the height n_w of the wall-adjacent cell: i. provides a sufficiently high mesh resolution in the normal direction n to the surface in order to adequately resolve the gradients of flow parameters, ii. complies with the wall function requirement on dimensionless wall unit $30 < n^+ = n_p u^*/\nu < 200$, being $n_p = n_w/2$ the cell center height. In the present study, a further need rises in relation to computational efficiency, because of the huge number of simulations required by the optimization process. For analogous accuracy, efficiency is pursued by cost saving made possible by relatively coarse computational mesh. The requirement (i) is satisfied when the n_w is as small as possible. Conversely, the requirement (ii) suggests large n_w. The second requirement is setting the range from which n_w can be chosen. To find the best value of n_w, a preliminary study on mesh dependency was carried out. First, the finest grid which satisfies the requirements (i) and (ii) was selected, i.e. $n^+ = 30$. Subsequent increasing mesh coarsening was considered, until the significant change in the results occurred, or the limit of $n^+ = 200$ was violated. The retained value of the cell height $n_w = 0.0125H$ was judged as a satisfying compromise among requirements, being the changes of the main aerodynamic metrics in the range from 2% to 5%. For the sake of conciseness, the grid sensitivity study is not detailed herein, this not being the main topic of the study. The automatic mesh generation within the optimization procedure is carried out by a script controlling blockMesh utility within OpenFoam©. To simplify mesh generation and to assure high mesh quality, barrier is modeled as a plate with nil thickness. In the face of changes of the barrier geometry, constant density of the cells closely upwind and downwind the barrier, and a maximum cell aspect ratio at the inlet and outlet equal to 100 are enforced. The total number of cells depends on the geometry of the barrier around which mesh is created, and ranges from 30,000 to 50,000.

The Finite Volume open source code OpenFoam© is used to numerically evaluate the flow-field. The cell-centre values of the variables are interpolated at face locations using the second-order Central Difference Scheme for the diffusive terms. The convection terms are discretized by means of the so-called Limited Linear scheme, a 2nd order accurate bounded Total Variational Diminishing (TVD) scheme resulting from the application of the Sweby limiter (Sweby, 1984) to the central differencing in order to enforce a monotonicity criterion. The SIMPLE algorithm is used for pressure-velocity coupling. The resulting computational

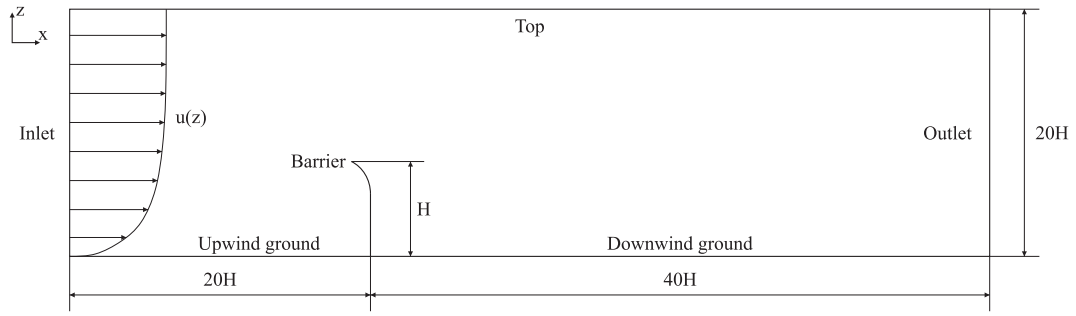

Fig. 2. 2D computational domain (not in scale). All the lengths are given in relation to barrier height H. $u(z)$-line represents the incoming logarithmic velocity profile.

model requires in average 15 min for a single simulated case on Intel(R) Core(TM) i7 CPU 860 @ 2.80 *GHz* with 3 cores employed.

3. Optimization approach

In mathematical terms optimization is a process of minimizing (or maximizing) a goal function $G(\mathbf{x})$, where $\mathbf{x}$ is the design variable vector, while satisfying constraints on design variables and responses (Boyd and Vandenberghe, 2004):

$$\begin{aligned} &\text{minimize} \;:\; G(\mathbf{x}) \\ &\qquad\quad \mathbf{x} \in \mathbb{R}^n \\ &\text{subject to} \;:\; U \geq (or =)\, f_i(\mathbf{x}) \geq (or =)\, L \;\; where \;\; i = 0, 1, \ldots, M \end{aligned} \tag{5}$$

where f_i is one of M numbers of constraints with its upper limit U and lower limit L. For a vector of design variables to be valid, it has to satisfy all the linear/non-linear equality/inequality constraints.

3.1. Bluff body aerodynamic optimization: state-of-art and specific features of present application

In the following, the main features of the optimization approaches adopted up to now in wind engineering applications are briefly reviewed. Then, the main features of the implemented optimization approach are given.

In all the studies cited in Section 1, the overall computational cost-saving objective is pursued by adopting Surrogate-Based Optimization (SBO). In SBO, a relatively inexpensive surrogate function replaces the objective function which is expensive to evaluate by computational simulations. The search for the optimum is therefore carried out on the surrogate model, which has to be previously constructed based on an adequate number of runs of the original function (Bernardini et al., 2015). The type of surrogate model and its fitting to the application case, the total number of the sampling points to calibrate it and their distribution on the sampling plan are obviously of paramount importance, and can drastically affect the overall accuracy of the optimization process (Queipo et al., 2005; Forrester and Keane, 2009). Different surrogates are employed in wind engineering applications: basic Kriging (Bernardini et al., 2015; Cid Montoya et al., 2018b), Multi-fidelity co-Kriging (Ding and Kareem, 2018), Artificial Neural Network based surrogate (Elshaer et al., 2017). The sampling plan results from point random generation (e.g. Elshaer et al., 2017) or optimal Latin hypercube sampling (e.g. Bernardini et al., 2015). The number of sampling points significantly varies from 15 in Bernardini et al. (2015) and Cid Montoya et al. (2018b) up to 200 in Elshaer et al., 2017.

In all the studies cited above, Genetic Algorithm Optimization (GAO) is preferred a priori to Gradient-Based Optimization (GBO) because of its general robustness in handling very large design spaces characterized by irregular landscapes with multiple local minima and/or discontinuities. To compensate the relatively high number of function evaluations required by GAO with respect to GBM, they are used at affordable costs thanks to the inexpensive solution of the surrogate model.

In the cited studies most of the optimizations are performed using multiple goal functions (e.g. Bernardini et al., 2015; Elshaer et al., 2017; Ding and Kareem, 2018; Karthik et al., 2018) defined directly from the simulated aerodynamic metrics, e.g. drag and lift coefficients and their fluctuations. Conversely, in Cid Montoya et al. (2018a) a single goal function is evaluated as the sum of the volume of bridge components while the aerodynamic metrics are taken into account as design variables.

In the present study, optimization is carried out on Computational Fluid Dynamics simulations. Surrogate models are not adopted because their accuracy strongly depends on a number of technical features and because of the relatively low computational cost of the function evaluations in the present application. The optimal design of dozen-kilometer long Sand Mitigation Measure implies minimizing costs and maximizing performance as two competing objectives. In other words, the cost is set as important as the performance in the perspective of a large-scale production, and the problem has an intrinsic multi-objective nature. In the present study, a single goal function is defined as the barrier cost-to-performance ratio. The adopted formalism allows to properly retain the multi-objective feature of the problem, even if multiple goal functions are not explicitly adopted. Two different optimization methods are used. If the response of the goal function is monotonic and continuous, GBO is selected because of its fast convergence. Conversely, if the response of the goal function contains multiple local minima, GAO is preferred.

3.2. General workflow of aerodynamic optimization

All the essential parts of the optimization process are combined in a workflow schematically shown in Fig. 3. The process is split into 4 main parts.

In pre-processing, the numerical mesh is automatically generated from the design variables. In the CFD part, wind flow is simulated around the barrier geometry. In the post-processing part, the relevant flow fields are used to evaluate the aerodynamic metrics and the goal function. The optimization part is the only part which significantly changes for different optimization methods. The complete optimization loop stops when either convergence criterion is met and optimal geometry is found, or the maximum number of function evaluations set in the stopping criterion is reached. In this study, the convergence threshold is set on the weighted residual of the goal function and equal to $1e-4$ for three successive iterations. The maximum number of function evaluations is set equal to 25 for GBO, and 100 for GAO. Conversely, a new set of variables is chosen based on the specified algorithm. Additional geometric constraints are checked to verify that the new set of variables satisfies them. The geometrically valid set of variables enters the new iteration of the loop. The optimization algorithms in the presented study are carried out with the open-source optimization toolbox Dakota© (Adams et al., 2014).

3.3. Gradient-Based Optimization

Gradient-Based Optimization is a popular local method which ex-

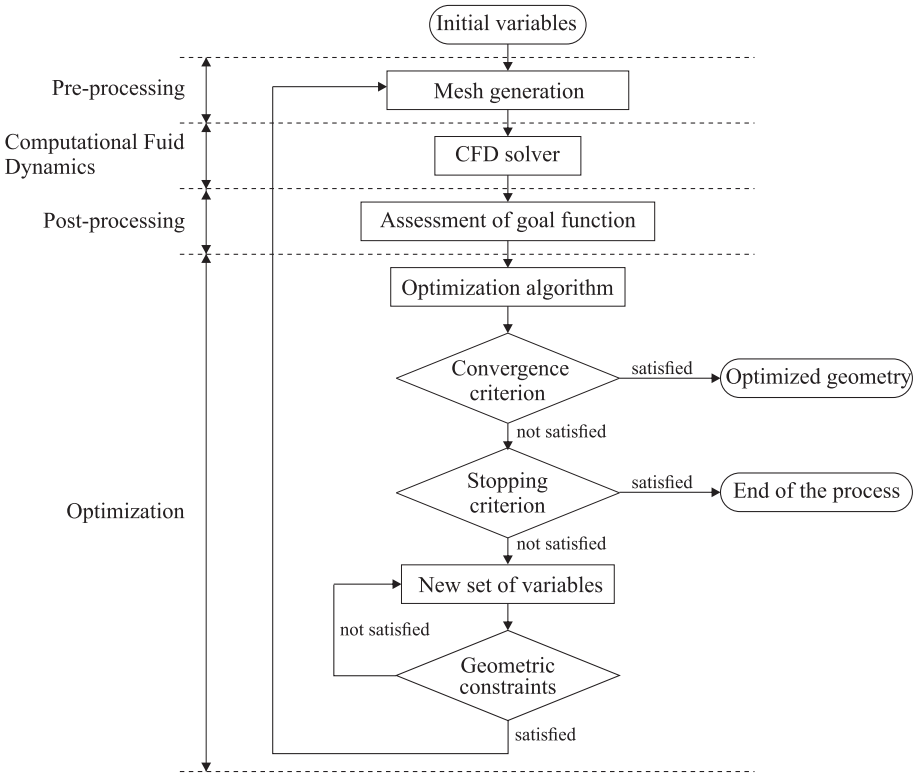

Fig. 3. Workflow of the optimization process.

ploits gradients of goal function to reach the local minimum. In the study, a common adaptation of the GBO called Method of Feasible Directions is used. GBO algorithms are best suited for efficient navigation to a local minimum in the vicinity of the initial point. The two main steps of GBO, i.e. calculation of gradient and stepping in the direction of the gradient, can be defined in mathematical terms as:

$$\nabla G\left(\mathbf{x}\right) = \left(\frac{\partial G(\mathbf{x})}{\partial x_1}, \frac{\partial G(\mathbf{x})}{\partial x_2}, \ldots, \frac{\partial G(\mathbf{x})}{\partial x_n}\right)$$
$$G(\mathbf{x})_{i+1} = G(\mathbf{x})_i - \eta \nabla G(\mathbf{x}). \tag{6}$$

where $G(\mathbf{x})$ is the goal function, $\mathbf{x}_0$ is the initial point, and η is the gradient step. The gradient step is always a positive real number that allows the progression from the initial point x_i to the new point x_{i+1}. In the study, $\eta = 0.05$ is adopted.

3.4. Genetic algorithm optimization

Genetic Algorithm Optimization is a global method which mimics the Darwin's theory of evolution (for more details, interested readers can refer to Simon, 2013). There are several applications of GAO coupled with CFD analysis in the environmental engineering literature (e.g. Ooka et al., 2008; Gosselin et al., 2009; Xue et al., 2013). The workflow of GAO adopted in the study is shown in Fig. 4.

The initial steps consist of the selection of a random initial population and the assessment of the goal function for each individual. The population size is one of the main parameters affecting computational cost and convergence, and in this study is set equal to 10. Reproduction includes crossover and mutation processes, which takes place in the following order: i. crossover is applied with a fixed probability on the chosen parents; ii. if crossover is applied, mutation is applied with a fixed probability to new individuals; iii. if crossover is not applied, mutation is applied with a fixed probability to the parents. The crossover rate specifies the probability of a crossover being performed to generate a new offspring. In this study, mutation is performed by modifying the value of

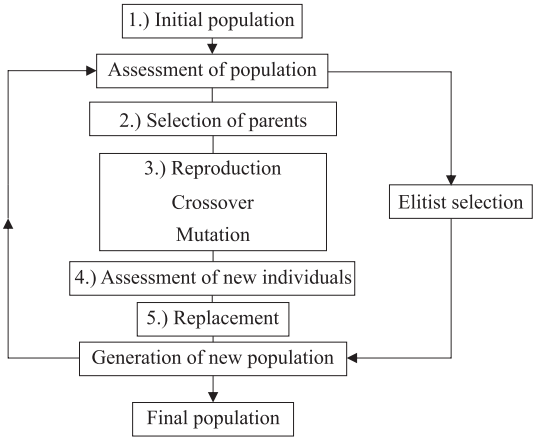

Fig. 4. Workflow of genetic algorithm optimization.

the design variables by a given percentage. After the reproduction process the goal function for newly generated offspring is evaluated. In the replacement process the current population and newly generated individuals are combined to create the new population. In the study, this is done in the form of the elitist selection. A defined number of the best individuals from the initial population are directly transferred to the new population. The remaining population is filled by the best offspring and remaining parents.

4. Set-up of the case study

In the following, incoming wind flow features adopted in the CFD simulations are reported first. Then, Shield for Sand conceptual design is briefly recalled, discussing its components and aerodynamic working principles. The concepts inspiring the construction development of the

barrier are introduced. Finally, the design variables arising therefrom are defined, together with their industrial constraints. The performance and cost metrics are defined, and the optimization goal function is set.

4.1. Features of the incoming flow

The incoming wind flow reflects actual desert conditions. The far-field aerodynamic roughness at the inlet is set equal to $z_0 = 1e-2$ m, while the ground aerodynamic roughness of the upwind and downwind strips is set equal to $z_{0,g} = 1e-3$ m because of grading of the ground in the neighborhood of the infrastructure. The far-field wind shear velocity is set equal to $u_* = \sqrt{\tau/\rho} = 0.82$ m/s, where τ is the shear stress at the ground surface. Such a value of u_* is appropriately chosen in order to exceed the mean value of the threshold shear velocity u_{*t} for sand grain diameters in the range $d \in [0.063, 1.2]$ mm, i.e. windblown sand transport occurs upwind the barrier. u_{*t} is classically defined as the minimum value of the wind shear velocity above which sand transport occurs and basically depends on d (Shao, 2008). In the present study, the mean value of u_{*t} is obtained from Raffaele et al. (2016), where its full statistical description is provided. In this study, the sand diameter is set equal to $d = 0.5$ mm, i.e. a medium sand grain diameter. It results, $u_{*t} = 0.4$ m/s. The mean wind speed at the height $h_{ref} = 80$ m is equal to $u_{ref} = 18$ m/s. It directly follows that $Re_H = hu_H/\nu \in [1.7e+6, 3.7e+6]$ for a barrier height equal to $2 \leq H \leq 4$ m. Significant Re effects are not expected to take place, being Re_H widely within Reynolds supercritical regime, and having the selected barrier a high degree of bluffness.

4.2. Barrier conceptual design and construction development

The shape optimization is carried out on the patented Shield for Sand (S4S) solid barrier (Bruno et al., 2016). Fig. 5 shows the conceptual design (a) and a render (b) of S4S.

S4S cross-section geometry includes three components: (A) a generic foundation, (B) a lower quasi-vertical part, and (C) an upper windward concave deflector. The barrier overall height H depends on the specific construction site, namely the magnitude of the incoming sand drift. Each component ensures a specific functional requirement of the SMM. The foundation defies the overturning moment induced by the lateral wind load and the upwind trapped sand passive pressure. The quasi-vertical part allows an easy sand removal maintenance by means of sand removal machines, e.g. sand ploughs or sand blowers. The upper windward concave deflector ensures the S4S aerodynamic working principle. In particular, the deflector induces an upwind recirculation vortex that promotes the local downward deflection of the wind flow and reverses the flow close to the ground, decreasing u_*. As a result, sand sedimentation occurs upwind the barrier where $u_* < u_{*t}$ (Bruno et al., 2018b, a). In light of this, the upwind recirculation vortex behaves as a sand trapping vortex. The shape of the deflector is expected to deeply affect S4S aerodynamics: the shape has been obtained during the conceptual design by a heuristic approach; the deflector profile follows a spline line using multiple control points. The S4S geometry shown in Fig. 5(a) is retained as the baseline solution and referred by the label #0 in the following. It is characterised by $h/H = 0.33$ and $s/H = 1.12$.

Alternative construction methods and materials are expected not to affect the working principle of S4S, if the shape is unchanged. S4S construction development is addressed to construction simplicity and cost saving, while maintaining or improving aerodynamic performances. In order to obtain such a goal, the deflector is obtained by using one or more self-supporting panels, available as semi-finished steel products. Each panel has a constant radius of curvature. Analogously, the reinforced concrete (r.c.) direct foundation and vertical wall are precast as a single L-shaped retaining-type wall.

4.3. Optimization set-up

The total height of the barrier is kept constant and equal to H, in order to carry out a pure shape optimization. Two alternative design solutions are considered, as sketched in Fig. 6 (a) and (b). In both of them, the vertical wall extends from control point P_0 to P_1. The original spline-like deflector is replaced by $N = 1$ and $N = 2$ circular arcs, each extending from P_i to P_{i+1} control points ($i = [1,N]$). In the figure, all the geometrical parameters are detailed. Among them, the height of the vertical wall h and the arc lengths of the plates s_i are retained as *design variables*, while the central angles α_i, tangency angle α_t, radii r_i and overall curvilinear

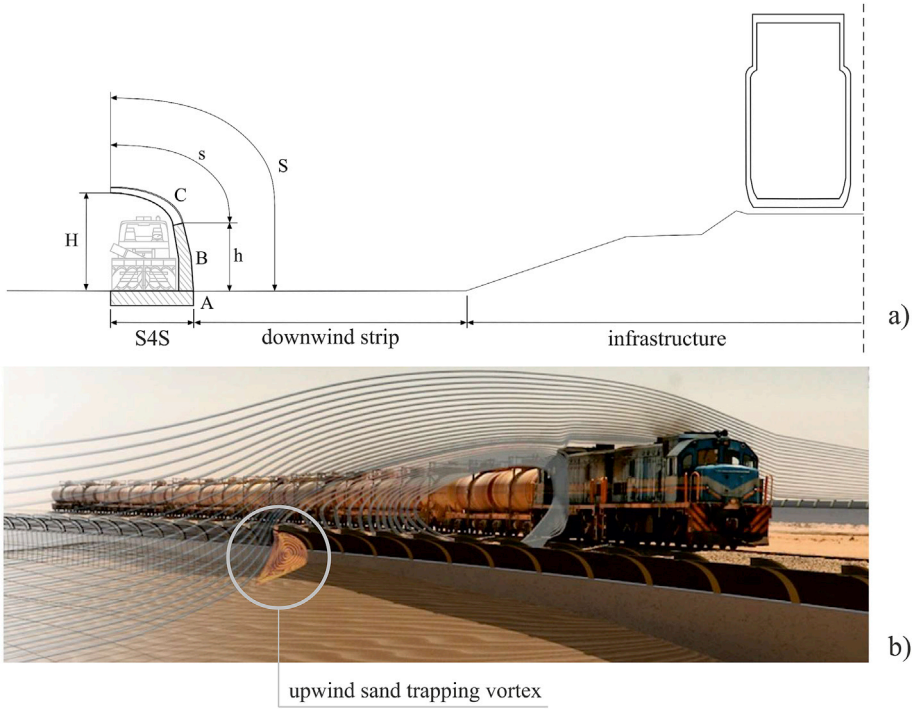

Fig. 5. Shield for Sand conceptual design (a) and a render of S4S along a desert railway line (b).

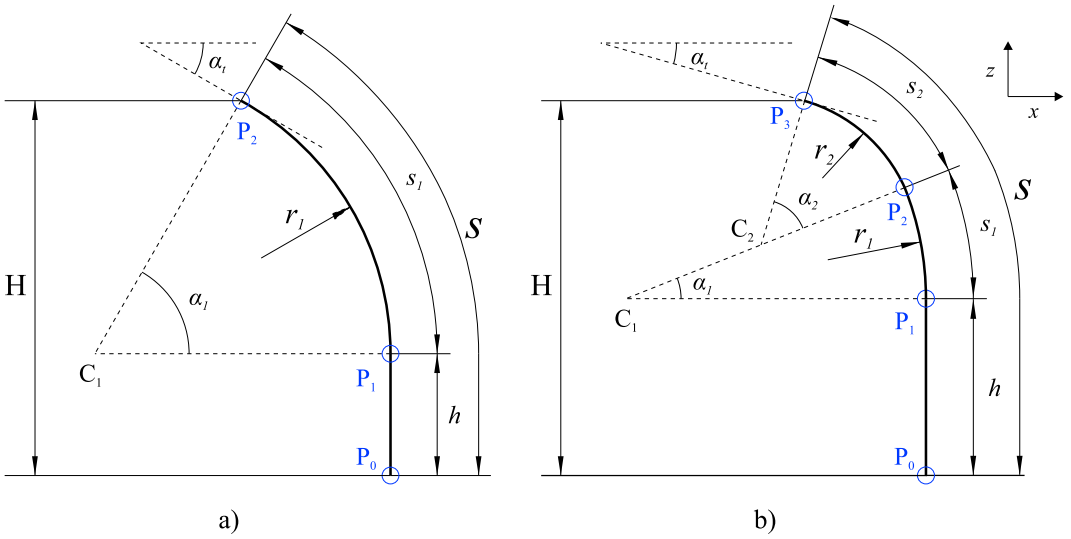

Fig. 6. Above ground geometrical setup with one (a) and two (b) steel panels.

length S are *derived parameters*. *Geometrical constraints* are introduced to discard undesired shapes, and to ensure the functionality of the barrier. Vertical wall and adjacent arcs share common tangent lines at control points P_i, to ensure the barrier smooth shape. The design variables are constrained directly within the following ranges: $0.18 \leq s_i/H \leq 0.53$ and $0.325 \leq h/H \leq 0.65$, where the lower bound on h allows unobstructed sand removal. Additional constraints are imposed on derived parameters: i. $S = h + \sum_{i=1}^{N} s_i \geq H$, ensuring the total curvilinear length S of the barrier to be longer than or equal to its height H; ii. $\sum_{i=1}^{N} \alpha_i \leq \pi/2$, ensuring that the height of the free end of the deflector is equal to H. *Manufacturing constraints* apply to r_i in order to allow cold bending ($r_i \geq r_m$, being $r_m = 634$ mm), and to the thickness of the steel panels t_i to obey to product standardization discrete values.

The *goal function* is generally defined as $G = c/p$, where c and p are the barrier cost and performance metrics, respectively. The sand trapping *barrier performance* p during preliminary design are estimated by means of purely aerodynamic metrics, namely the friction velocity u_*. As the wind approaches the barrier, u_* reduces in magnitude. The sedimentation point takes place on the upwind ground surface where $u_* = u_{*t}$, the inflection point where the separation of the boundary layer occurs and $u_* = 0$, while the stagnation point on the barrier upwind surface is classically defined as the point where $u_* = 0$ (Fig. 7a). In the light of this, the sedimentation length L_{sx} is defined as the distance between the sedimentation point at the ground and the foot of the barrier, and L_{sz} corresponds to the height of the stagnation point. A_s is defined by the area bounded by the profile of the barrier below the stagnation point, and the sedimentation length, i.e. $A_s \propto L_{sx} L_{sz}$. As proven in Bruno et al. (2018c), A_s is linearly proportional to the recirculation area $A_r \propto L_{rx} L_{rz}$ (Fig. 7a), where L_{rx} and $L_{rz} = L_{sz}$ are the along-wind horizontal and cross-wind vertical dimensions of the upwind sand trapping vortex, respectively. In the present study, the barrier performance is approximated as $p \approx A_r$.

The overall *barrier cost*, among others, includes shipping, labour, and

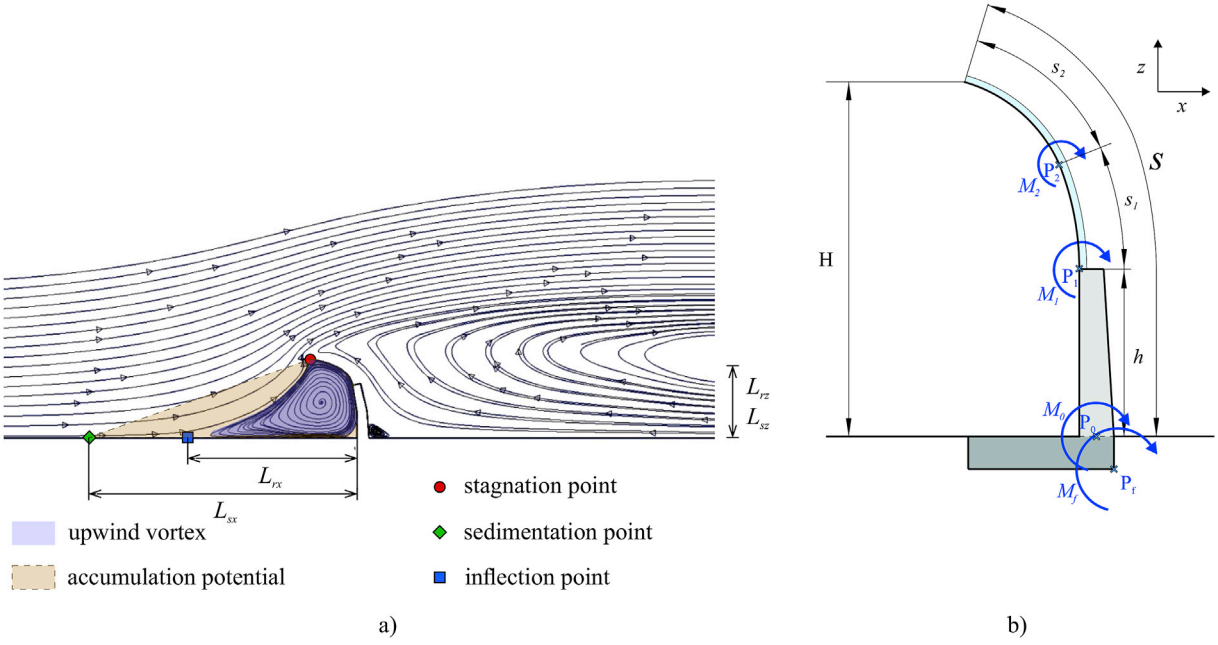

Fig. 7. Mean streamlines around S4S baseline solution, flow structures and characteristic lengths of the local flow, after Bruno et al., 2018b (a). Structural parameters, with wind-induced bending and overturning moments (b).

material costs. Such costs depend to a different extent on actual, specific site, and industrial and economic scenarios. Material costs are the less variable. For the sake of generality and comparability, the optimization is carried out by considering the cost of materials only, and by scaling to the baseline solution. The barrier cost c follows from the cost of materials per unit weight, and from barrier total weight. The ratio between the steel unit cost and the reinforced concrete unit cost is set $c_s/\ c_{rc} = 44$. Weights follow from sizing of the elements, that mainly depends in turn on wind-induced loads, and trapped sand passive pressure. In the present study, the aerodynamic wind loads are considered only, coherently with the aerodynamic-based optimization. The wind-induced design bending moments M_i and design overturning moment M_f are assessed at pivot points P_i, for $i = 0, 1, 2$, and P_f, respectively (see Fig. 7b). Clearly, the higher M_i and M_f, the higher the construction cost c. Component cross-sections and global equilibrium have been verified by referring to EN 1991-1-4 (2005). Design moments are assessed by means of the peak velocity pressure q_p related to the basic wind velocity $u_b = 30$ m/s, and wind exposure factor $c_e(z) = 1 + 7/\ln(z/z_0)$. Wind load partial safety factor is set equal to $\gamma = 1.5$, while steel resistance partial safety factor is set equal to $\gamma_s = 1.05$.

For the sake of generality, in the following all design variables and results are made dimensionless by referring to the scale quantities H (height of the barrier), u_H (incoming wind speed at the barrier height), ρ (air density). Moreover, performance and cost metrics, as well as the goal function, are normalized by referring to the corresponding quantities of the baseline solution in order to highlight relative optimization.

5. Preliminary sensitivity study

A systematic sensitivity study is carried out before optimization. First, it is intended to provide a sound phenomenological insight in the effects of the design parameters on the flow field. Second, it aims at evaluating the trend of the performance and cost, as well as of the goal function, and at recognizing emerging trends versus other parameters, if any. Third, the sensitivity study is carried out to select a priori the most suited optimization method in the light of the trend of the goal function, and to prove a posteriori that the optimization converges to the optimal solution. The preliminary sensitivity study is carried out for both alternative design solutions ($N = 1$ and $N = 2$). It adopts as design parameters the same quantities selected as design variables within the optimization process.

5.1. Preliminary sensitivity study for $N = 1$

Fig. 8 shows the sampling plan of the design parameters h and s_1. The sampling covers the ranges $0.325 \leq h/H \leq 0.65$ and $0.35 \leq s_1/\ H \leq 0.53$ by uniform discrete steps $\Delta_h/H = 0.025$ and $\Delta_{s1}/H = 0.05875$. 17 valid

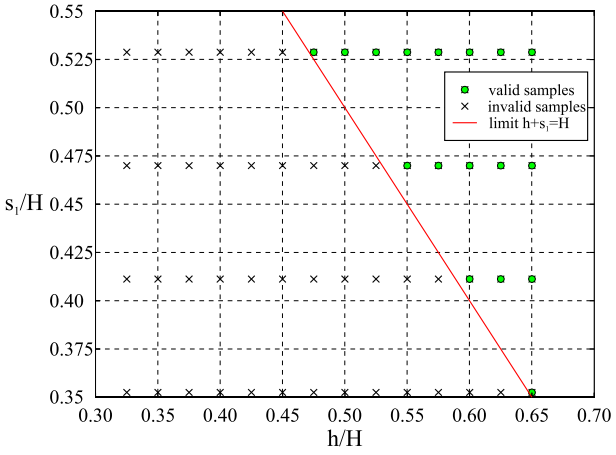

Fig. 8. $N = 1$ - Sampling plan for sensitivity study.

cases result when all the constraints are satisfied.

Fig. 9 collects fields of some flow variables relevant to the barrier performances, with reference to three samples. Sample #1 has a low overall curvilinear length very close to H ($s1/H = 0.353$ and $h/H = 0.65$). In other terms, its geometry is the closest to the Straight Vertical Wall (SVW) limit case ($s1/H + h/H = 1$) among the evaluated samples. Sample #3 is the one with maximum curvilinear length ($s_1/H = 0.53$ and $h/H = 0.65$). Finally, sample #2 is an intermediate case between the above ($s_1/H = 0.41$ and $h/H = 0.625$). Fig. 9(a) shows the mean streamlines in a wide region around the barrier. Two main coherent flow structures are recognized: an upwind vortex and a very large downwind vortex, that extends over about $15H$ in the wake. Whilst the downwind vortex does not significantly vary, both the $x-$ and $z-$ wise size of the upwind vortex depends on the design parameters. Corresponding erosion and sedimentation zones along the ground level complement the figure. They are assessed depending on whether u_* is higher or lower than u_{*t} ($u_{*t} = 0.4$ m/s for a mean sand grain diameter equal to $d = 0.5$ mm). Fig. 9(b and c) show a close-up view around the barrier comprising the upwind vortex in terms of mean streamlines of the wind flow (b) and contours of the turbulent dissipation rate ω filled by vorticity color map (c). Beside the outer quasi-irrotational free flow (green streamlines, nil ω) and the upwind and downwind main clockwise vortices (red and blue streamlines, low ω), both streamlines and ω contours point out in detail the small secondary vortex downwind the barrier (orange streamlines, very low ω), and the shear flow (yellow streamlines, high ω) corresponding to the attached and separated boundary layer. The boundary layer is initially attached to the ground surface upwind the inflection point; it is separated adjacent to the upwind vortex (between the inflection and the stagnation points); then reattached along the upper part of the barrier upwind surface (between the stagnation point and the barrier free end); finally separates at the sharp edge of the barrier free end. Recirculating flows have significant effect on windblown sand transport. In fact, vortices modify both magnitude and direction of the wind shear velocity u_*. The sedimentation lengths L_{sx} and L_{sz} as well as recirculation lengths L_{rx} and L_{rz} progressively increase from sample #1 to sample #3 thanks to the windward migration of the sedimentation point and the upward migration of the stagnation point.

Wind-induced pressure field on the barrier is clearly relevant to wind action and to the barrier structural sizing and cost in turn. Fig. 10 (a) and (b) show the distributions of the aerodynamic pressure coefficient $C_p = \frac{p-p_\infty}{1/2\rho u_H^2}$ along upwind and downwind surfaces of the barrier, respectively. C_p distributions for every sample are sorted for increasing values of s_1/H, and emphasis is given to the samples selected in Fig. 9.

Generally speaking, the mean pressure along the barrier surfaces is directly related to the curvature of the time-averaged flow streamlines along the same surface, i.e. the shape and the length of the recirculation regions (Bruno et al., 2014). The C_p distribution along the downwind surface is almost constant and does not change significantly by varying the design parameters (Fig. 10b), consistently with the nearly constant shape and size of the downwind main vortex. Only a slight pressure recovery takes place along the upper part of the rear surface ($z/H > 0.7$) for deflectors significantly curved ($s_1/H > 0.41$, e.g. samples from #2 to #3). The C_p distribution along the upwind surface (Fig. 10a) is mainly characterized by the height of the stagnation point, i.e. by the abscissa z where the maximum pressure occurs along the upwind surface. The curve corresponding to sample #1 identifies the stagnation point at the lowest height among other samples. As the curvilinear length increases, the stagnation point moves towards the top of the barrier. Sample #3 induces the highest stagnation point, almost at the deflector free-end. It is worth recalling that the stagnation point of the baseline conceptual design of S4S nearly corresponds to the deflector free-end ($z = H$, Bruno et al., 2018b). Below the stagnation point (i.e. along L_{rz}), the upwind vortex is adjacent to the upwind surface, and C_p is almost constant and independent from the design parameters. Above the stagnation point and up to the deflector free-end, the boundary layer is reattached, the flow just

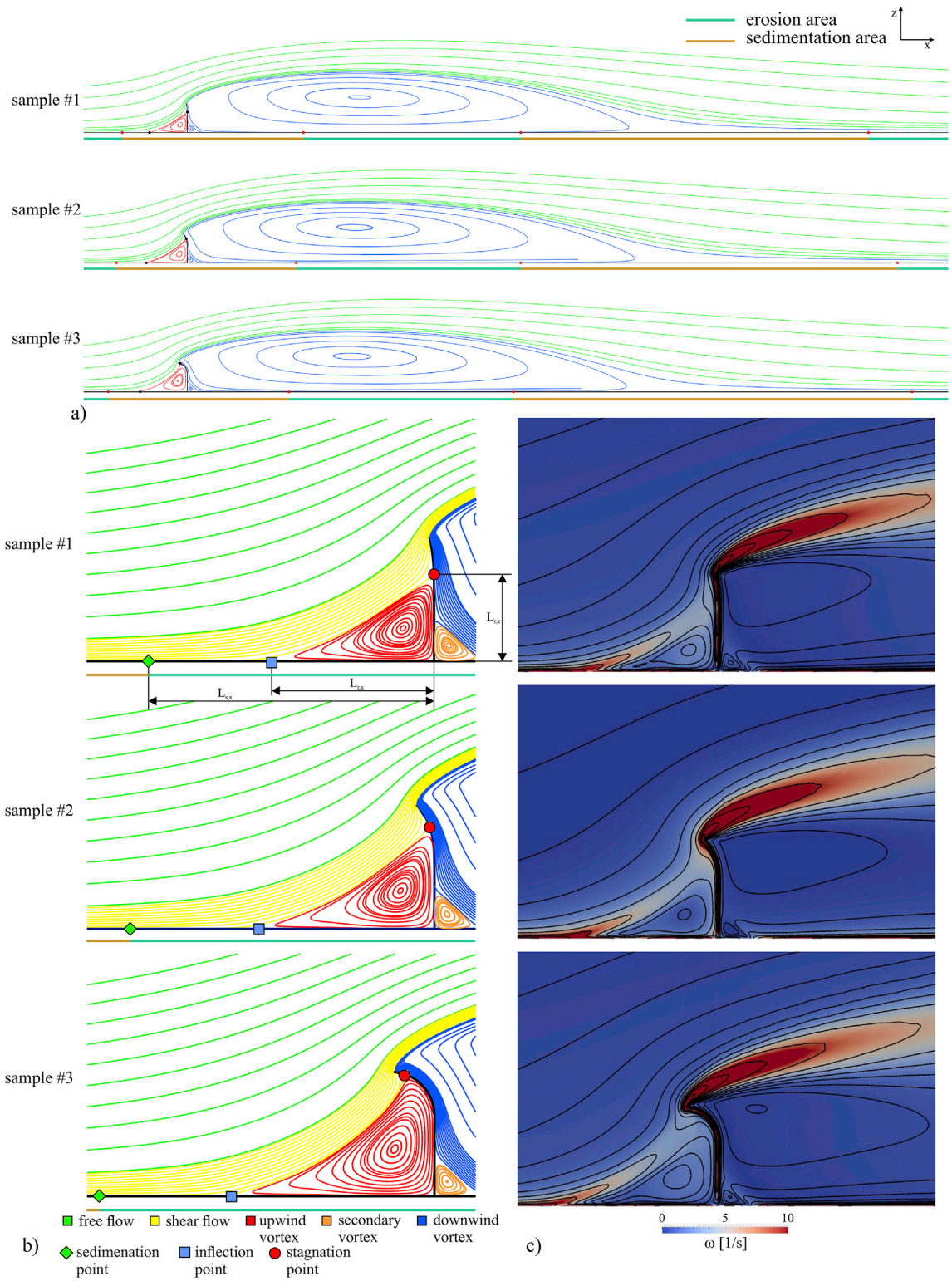

Fig. 9. $N = 1$ - Flow structures and characteristic quantities around differently shaped barriers: limit case close to SVW (a), example between two limit cases (b), most deflected simulated case (c).

outside it is progressively accelerated, and the C_p progressively decreases because of the very classical Bernoulli's law. In short, the higher the stagnation point, the longer the upwind surface exposed to high and z-wise constant pressure distribution.

In order to discuss more concisely the effects of the design parameters s_1 and h, let us move now from the local quantities above to bulk performance metics (Fig. 11) and cost metrics (Fig. 12). $L_{rx}/\ L_{rx,0}$, $L_{rz}/\ L_{rz,0}$ and $A_r/A_{r,0}$ are plotted versus s_1/H and h/H in Fig. 11(a), (b) and (c), respectively.

The longest L_{rx} and L_{rz} result from the highest curvilinear length of the barrier S. The rate of increase of L_{rz} is higher than the one of L_{rx} versus both design parameters: high vertical wall and long curved deflector effectively rise the stagnation point, while their effect is less dramatic, even if still significant, in moving the inflection point windwards. Overall

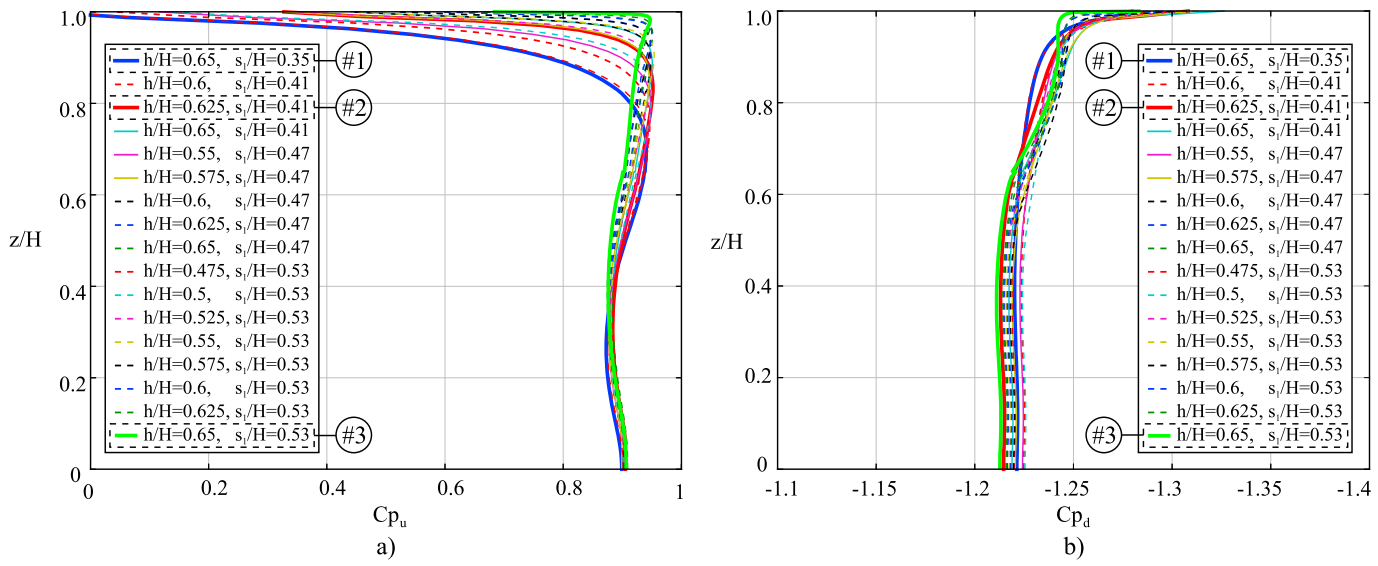

Fig. 10. $N = 1$ - Pressure coefficient over barrier height: Upwind surface (a), Downwind surface (b).

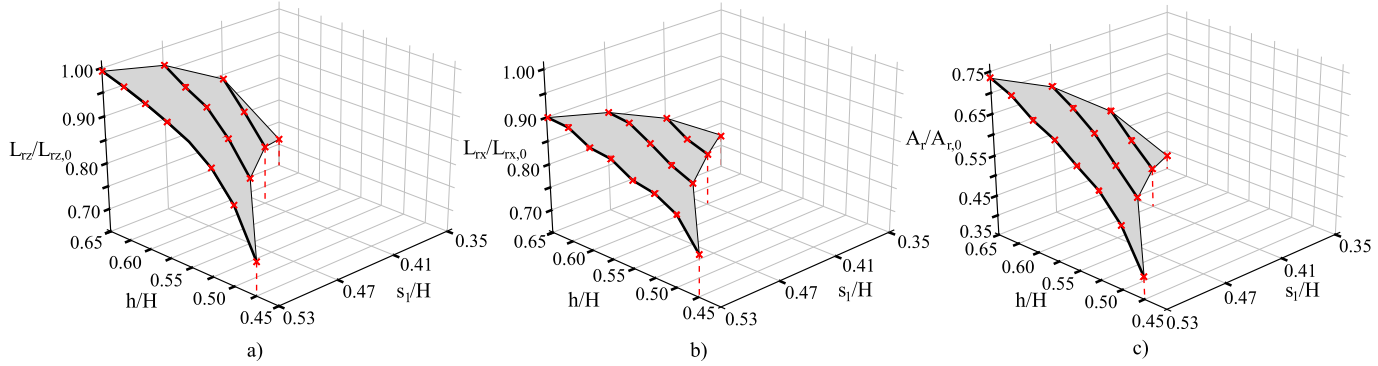

Fig. 11. $N = 1$ - Bulk metrics related to performance: along-wind projection L_{rx} (a), vertical projection L_{rz} (b), and recirculation area A_r (c) of the upwind sand trapping vortex.

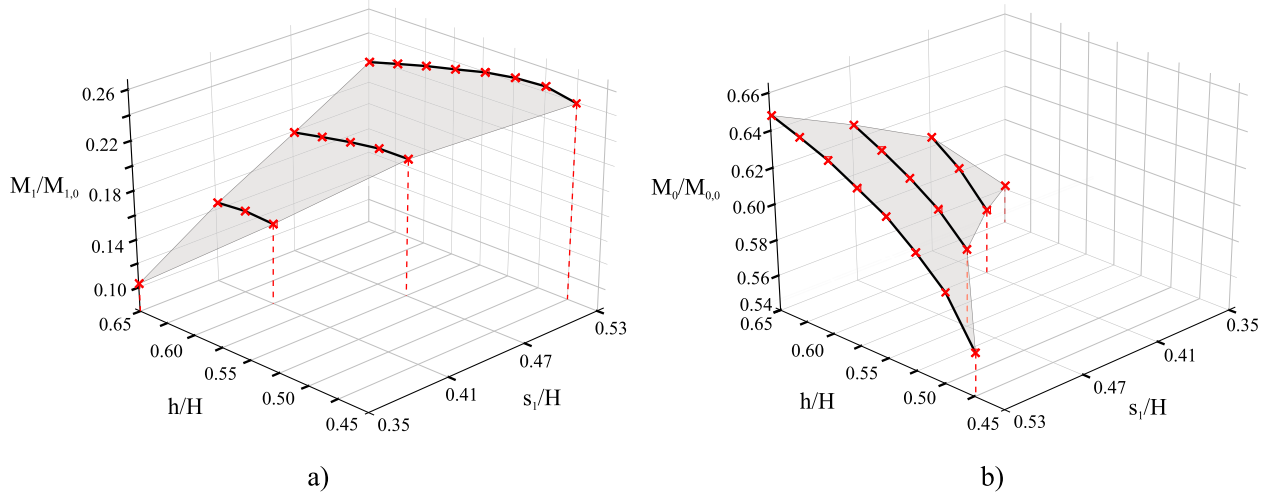

Fig. 12. $N = 1$ - Bulk metrics related to cost: Moment M_1 at the deflector base (a), overall base moment M_0 (b).

results are encouraging for each single recirculating length (Fig. 11a, b): the adoption of a single plate allows to nearly approach the baseline performances, i.e. $L_{rz} \approx L_{rz,0}$ and $L_{rx} = 0.9L_{rx,0}$. However, a significant relative performance gap remains in terms of A_r (Fig. 11c), being $0.5 \leq A_r/A_{r,0} \leq 0.75$. The normalized aerodynamic moments $M_1/M_{1,0}$ and $M_0/M_{0,0}$ are plotted versus s_1/H and h/H in Fig. 12(a) and (b),

respectively.

M_1 linearly increases as s_1 increases, while it is nearly constant versus h. In other terms the deep and almost constant suction versus s_1 along the downwind surface (Fig. 10b) largely prevails on the pressure reduction along the deflector upwind surface (Fig. 10a), and the magnitude of M_0 is mainly due to the extent of the curvilinear abscissa over which integration is carried out. Conversely, M_0 shows a quadratic trend versus both s_1 and h. The reason of such a trend is manifold. For sure, both the resultant aerodynamic force and its lever arm are proportional to the whole curvilinear length of the barrier over which pressure is integrated. Moreover, also the height of the stagnation point is a quadratic function of both s_1 and h (Fig. 11a): the higher the stagnation point, the longer the curvilinear length of the upwind surface subjected to high and constant pressure (Fig. 10a). Once more, overall results about aerodynamic moments are encouraging: wind forces are significantly lower than in the baseline solution, being $0.1 \leq M_1/M_{1,0} \leq 0.25$, and $0.55 \leq M_0/M_{0,0} \leq 0.65$.

The complete set of samples assessed within the sensitivity study for the case $N = 1$ are shown on the plane c/c_0-p/p_0 in Fig. 13(a), together with the streamlines around selected samples in Fig. 13(b). Each circle corresponds to a sample. Its size and filing color correspond to derived parameters: size is proportional to the overall curvilinear length S of the barrier; filling color corresponds to the amplitude of normalized circle angle $\alpha_1/90 = (90 - \alpha_t)/90$ of the deflector. The c/c_0-p/p_0 plane is divided into 6 regions based on the normalized values of cost, performance and goal function with respect to the S4S baseline solution #0 at coordinates $(1, 1)$ in the graph. The regions are labeled as $q_{i,j}$, where i represents the quadrant index and j a specific sector of the i-th quadrant. The quadrant q_1 includes samples characterized by higher cost and higher performance with respect to the ones corresponding to the baseline solution, i.e. $c/c_0 > 1$ and $p/p_0 > 1$. The quadrant q_2 includes samples characterized by higher cost and lower performance with respect to the ones corresponding to the baseline solution, i.e. $c/c_0 > 1$ and $p/p_0 < 1$. The quadrant q_3 includes samples characterized by lower cost and lower performance with respect to the ones corresponding to the baseline solution, i.e. $c/c_0 < 1$ and $p/p_0 < 1$. The quadrant q_4 includes samples characterized by lower cost and higher performance with respect to the ones corresponding to the baseline solution, i.e. $c/c_0 < 1$ and $p/p_0 > 1$. In short, quadrants q_2 and q_4 host the worst and best scenarios, respectively. First and third quadrants are further split according to the bisector corresponding to the isocontour $G/G_0 = 1$. The sub-quadrants $q_{1,1}$, $q_{1,2}$, $q_{3,1}$, $q_{3,2}$ result. In particular, $q_{1,1}$ and $q_{3,1}$ correspond to $G/G_0 < 1$, while $q_{1,2}$ and $q_{3,2}$ correspond to $G/G_0 > 1$. All samples belong to the third quadrant q_3, i.e. their performances are always lower than the ones of the baseline solution. However, results are encouraging in a genuine design perspective: cost-to-performance values lower than the baseline solution ($G/G_0 < 1$, sub-quadrant $q_{3,1}$) result from significant cost reduction, rather than performance growth. For all samples, the steel plate and r.c. wall thicknesses are equal to the ones of the baseline solution ($t_{s1}/t_{s,0} = 1$ and $t_h/t_{h,0} = 1$). Hence, the cost reduction results from shortening the overall curvilinear length, and by increasing the height of the vertical wall, because of r.c. cheap unit cost compared to steel. More interestingly, a clear and emerging direct proportion of G to the free-end tangency angle α_t can be observed, i.e. the lower α_t, the lower G. In other terms, when the deflector's free-end has horizontal tangent, the stagnation point moves up to the barrier free end at $z = H$. As a result, L_{rz} and A_r are the highest and G is the lowest (sample #3). Analogously, the shorter the radius of curvature and the longer the overall curvilinear length in turn, the lower G. In summary, a highly-bended one-piece deflector with horizontal free end allows to reduce the barrier cost-to-performance ratio.

Finally, the normalized goal function G/G_0 is plotted in Fig. 14 versus the original design parameters s_1 and h. By fixing alternatively h or s_1, G function is monotonically and smoothly decreasing versus the other design parameters. A well-defined minimum $\tilde{G}/G_0 = 0.79$ (red circle in Fig. 14) occurs at $h/H = 0.65$ and $s_1/H = 0.53$. Such a trend reflects the

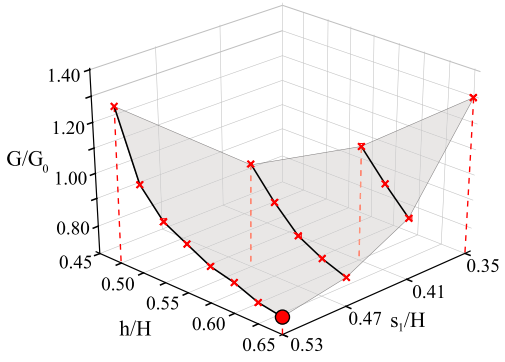

Fig. 14. $N = 1$ - Trend of the goal function versus the design parameters.

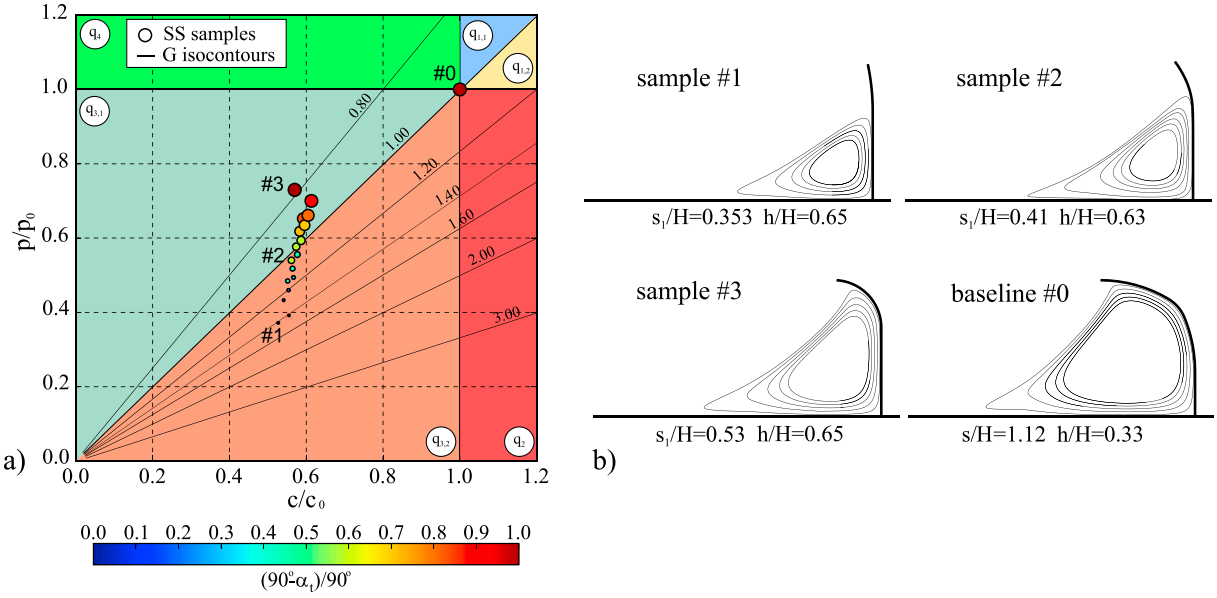

Fig. 13. $N = 1$ - Synopsis of the sensitivity study (SS): samples in the cost-performance plane (a), streamlines around selected samples (b).

phenomenological reading provided by Figs. 9 and 10. Changes of the design parameters do not involve a switch from an aerodynamic regime to another: the flow topology does not vary qualitatively, while changes occurs only in the size of the flow structures and related points, such as the stagnation and inflection coordinates. In short, the baseline S4S barrier is a high-degree-of-bluffness body, and the same holds in the whole design plane. In this sense, the current application is less challenging than the case studies in e.g. Cid Montoya et al. (2018b) or Ding and Kareem (2018), characterized by the transition from high-to low--degree of bluffness aerodynamics during the optimization process, and related non monotonic objective functions.

5.2. *Preliminary sensitivity study for* $N = 2$

In the light of the emerging dependency of the goal function on the free-end tangency angle α_t (Fig. 13, Subsect. 5.1), in the following $\alpha_t = 0$ is set as further geometrical constraint together with $S/H = s_1/H + s_2/H + h/H \geq 1$. This allows to reduce the number of design parameters from 4 to 3, namely h, s_1, s_2. The sampling of the design space covers the ranges $0.325 \leq h/H \leq 0.65$, $0.18 \leq s_i/H \leq 0.53$ by uniform discrete steps $\Delta_h/H = 0.025$ and $\Delta_{s_i}/H = 0.05875$. 429 valid cases result when all the constraints are satisfied. Bearing in mind the robustness of the aerodynamic behavior of the S4S barrier (Subsect. 5.1), the phenomenological insight of the effects of the design parameters on the flow field is not provided for $N = 2$, for the sake of brevity. Fig. 15, summarizes the results obtained from sensitivity study for $N = 2$ on the c/c_0-p/p_0 plane, analogously to Fig. 13.

Most of the samples still belong to the $q_{3,1}$ sub-quadrant (cost-to-performance values lower than the baseline solution), analogously to $N = 1$. Nevertheless, results are encouraging in the optimization perspective: a significant number of samples are located in the upper part of $q_{3,1}$ (say $0.9 \leq p/p_0 < 1, 0.7 \leq c/c_0 < 1$) and in the q_4 quadrant (lower cost and higher performance than baseline solution). These samples are remarkably clustered in two distinct point clouds. The high-cardinality cloud lies along the $G/G_0 = 0.8$ isocontour (e.g. samples #4, #5, #6 among others), while the low-cardinality cloud develops almost parallel to the former but shifted at higher cost and lower G/G_0 (e.g. samples #2 and #3 among others). It follows that samples having the same performance do not necessarily have the same value of cost-to-performance ratio (e.g. samples #2 and #6). On the one hand, such a finding confirms a purely performance-based optimization would only partially capture the whole nature of the design problem, and corroborates the choice of G/G_0 as goal function. On the other hand, the non trivial trend of the samples suggests a deeper insight on both performances and costs.

Overall, the performances ($0.6 \leq p/p_0 \leq 1.15$) are higher than in $N = 1$, and also higher than the baseline solution for about 30 samples ($p/p_0 > 1$). The performance is directly proportional to the overall curvilinear length S of the barrier, as clearly shown by size and filling color of the circles (Fig. 15a). However, barriers with the nearly same overall curvilinear length (e.g. samples #5 and #6, $1.45 \leq S/H \leq 1.46$) have different performances thanks to different shapes and resulting size of the trapping vortex.

The costs ($0.6 \leq c/c_0 \leq 0.95$) are higher than $N = 1$ as well, but still lower than the baseline solution ($c/c_0 < 1$). In the light of material unit costs, a higher vertical wall made of r.c. surely contributes to the overall cost reduction to parity of vertical wall thickness ($t_h/t_{h,0} = 1$ for all samples). However, barriers with the same r.c. vertical wall height and thickness (e.g. samples #3 and #4, $h/H = 0.65$) have different overall costs due to deflector. Indeed, all the samples in the low-cardinality cloud have the same maximum arc lengths ($s_1/H = 0.53$, $s_2/H = 0.53$), even if curvature varies (see e.g. #2 and #3 in Fig. 15b). The long span of the cantilever induces high aerodynamic moment M_1, thick steel plate adjacent to the r.c. wall ($t_{s1}/t_{s,0} = 1.2$), and high cost in turn. Conversely, the samples in the high-cardinality cloud (see e.g. #4, #5 and #6) have the steel plate thicknesses equal to the one of the baseline case ($t_{s1}/t_{s,0} = 1$ and $t_{s2}/t_{s,0} = 1$), and an overall cost lower than in low-cardinality cloud follows. Bubble plot in Fig. 16(a) shows the trend of sampled normalized goal function G/G_0 versus the design parameters h, s_1, s_2. For the sake of clarity of visualization, point style rather than their size varies to highlight different ranges of G/G_0. Fig. 16(b,c,d) plot G/G_0 versus two design parameters at the time, by setting constant values of the remaining parameter.

Overall, the range of variation of G/G_0 for $N = 2$ ($0.79 \leq G/G_0 \leq 1.1$) is narrower than for $N = 1$ ($0.79 \leq G/G_0 \leq 1.3$), thanks to the supplementary constraint on α_t. The trend of variation of G/G_0 remains quite smooth versus the design parameters, analogously to $N = 1$, thanks to the robust aerodynamic behaviour of the barrier. However, the trend is no longer fully monotonic, and local plateaux and minima occur. Even if a global minimum $\check{G}/G_0 = 0.79$ can be numerically assessed at $s_1/H = 0.53$, $s_2/H = 0.47$, and $h/H = 0.65$ (red circle in Fig. 16), multiple samples having $0.79 < G/G_0 < 0.82$ are highlighted in Fig. 16(a) by purple diamonds. They occur at relatively high values of h, s_1 and s_2, with an exception for the highest values of s_1 and s_2 ($s_1/H =$

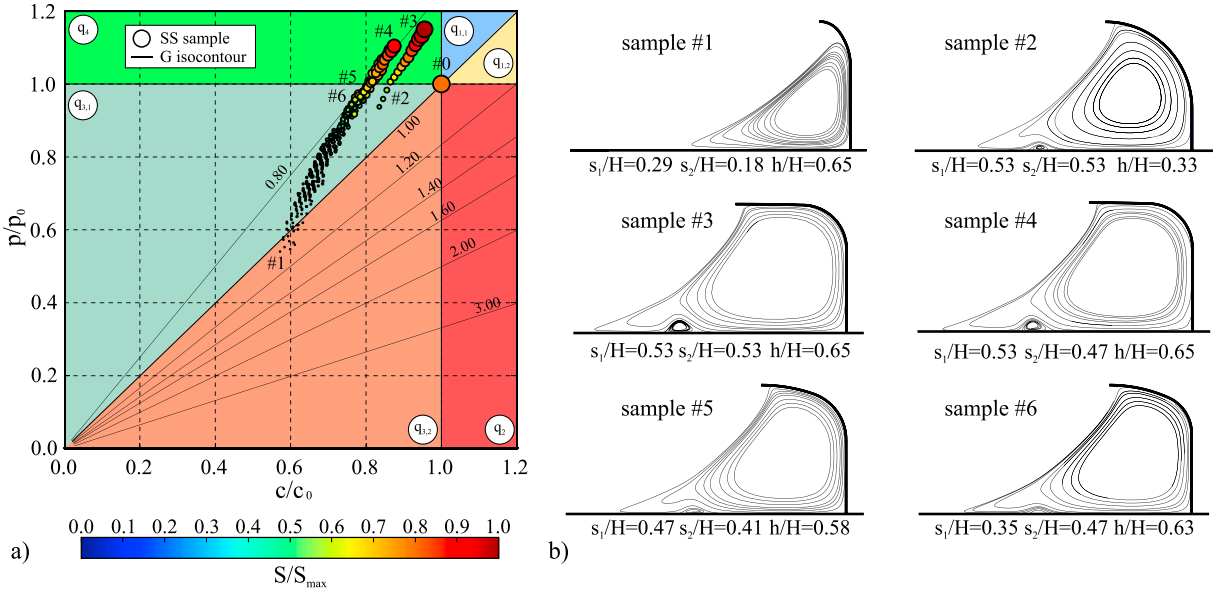

Fig. 15. $N = 2$ - Synopsis of the sensitivity study (SS): samples in the cost-performance plane (a), streamlines around selected samples (b).

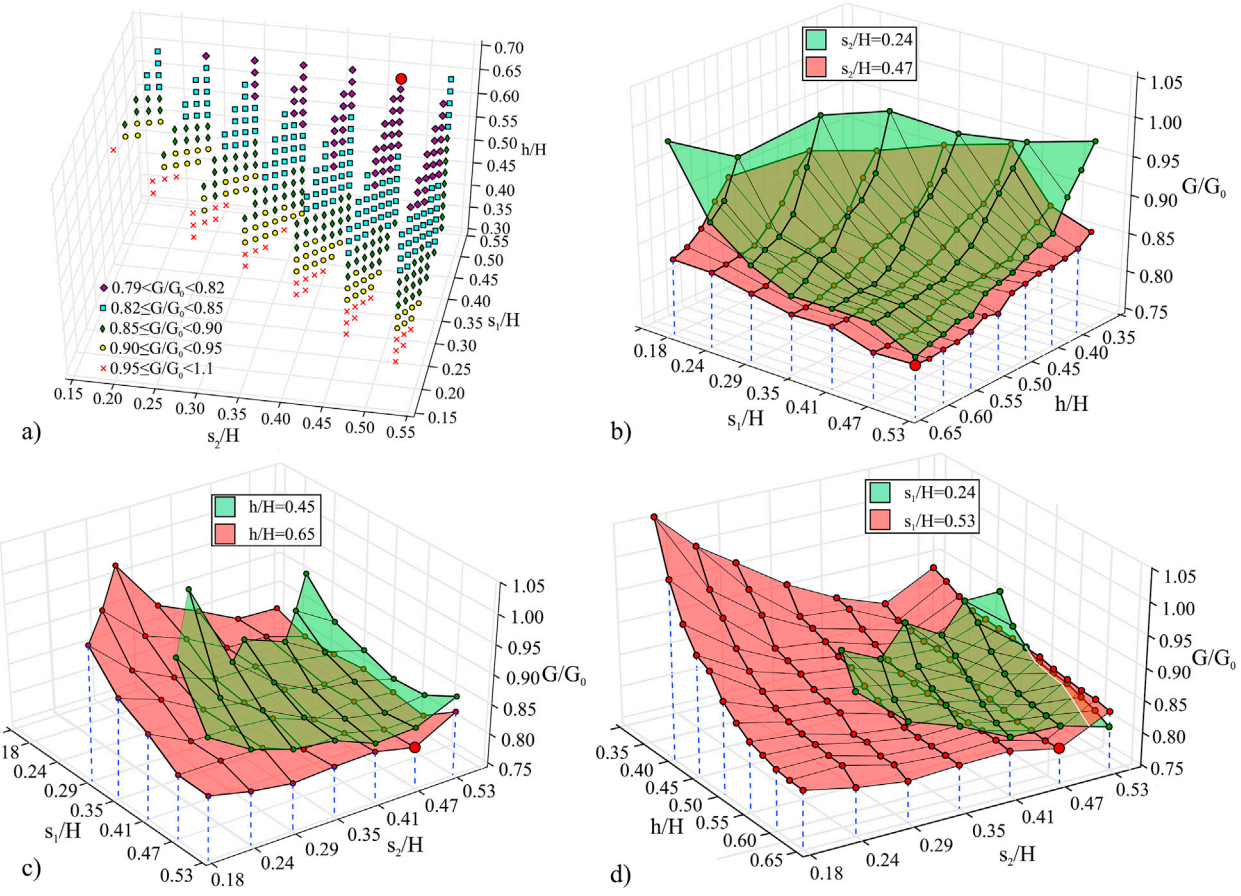

Fig. 16. $N = 2$ -Trend of the goal function in the overall design space (a), trend of the goal function versus pairs of the design parameters (b,c,d).

$s_2/H = 0.53$), where G/G_0 locally increases. Such varying trend results from the cumulated contribute of three design parameters instead of two as in $N = 1$. In the light of this, $N = 2$ case is more challenging than $N = 1$ in the optimization perspective.

6. Optimization

The optimization approaches used for $N = 1$ and $N = 2$ are selected a priori in the light of the trend of the sampled goal functions (Figs. 14 and 16, respectively). GBO is selected for $N = 1$ because of the monotonic and smooth trend of the goal function, making optimization affordable by this well established approach. Both GBO and GAO are employed for $N = 2$ to compare their accuracy and efficiency, bearing in mind the G function is no longer fully smooth and monotonic, and optimization is more challenging. In particular, two GBO runs are carried out to test its robustness depending on the initial solution.

Fig. 17(a) shows the trend of the dimensionless objective function versus the function evaluations for both $N = 1$ and $N = 2$. The sensitivity study also allows to estimate a posteriori the error along the optimization process by referring to the distance $\Delta_i = |\check{G} - \varphi_i| / G_0$ between the sampled minimum $\check{G} = 0.79$ and φ_i, where $\varphi_i = G_i$ for GBO, while $\varphi_i = \overline{G}_i$ and $\varphi_i = min(G_i)$ for GAO, being $\overline{G}_i$ and $min(G_i)$ the average and the minimum value of objective function over the individuals of the $i-$th population. Fig. 17(b) plots the distance Δ versus the iterations i.

As expected, for $N = 1$, GBO converges after 10 function evaluations only, and it reaches the sampled global minimum $\check{G}$, i.e. $\Delta_{10} = 0$ (Fig. 17b). For $N = 2$ and for any initial solution, it can be visually inferred that GBO reaches convergence plateaux with a high rate. However, the set convergence criterion is not numerically fulfilled because of the low convergence threshold, and the process progresses up to maximum number of evaluations for both runs. More interestingly, close but different G minima correspond to different initial solutions, namely $G/G_0 = 0.795$ and $G/G_0 = 0.804$ for first and second runs, respectively. In other words, as expected, GBO converges to local minima. However, the estimated error is in both cases lower than 2%. The trend towards convergence can be visually inferred also for GAO, although a larger number of function evaluations are required to qualitatively reach the plateau (about 50, Fig. 17a). The mean distance over the sixth population ($i = 6$, Fig. 17b) is of the same order of magnitude of the one obtained from GBO, while the minimum distance over the last population ($i = 10$) is equal to about 0.1%.

Fig. 18 displays the optimization paths disaggregating the goal function into cost and performance. Fig. 18(a) summarizes on the $c/c_0 - p/p_0$ plane the sample clouds from sensitivity analysis for reference. GBO and GAO successive evaluations along paths together with samples are shown on the same plane in Fig. 18(b,c,d). GAO populations 7th, 8th, and 9th are not plotted for the sake of clarity.

For $N = 1$, optimization starts from a poor initial solution straddling $q_{3,1}$ and $q_{3,2}$ sub-quadrants ($G/G_0 = 1$). The optimization path proceeds across $q_{3,1}$ mainly increasing performance, and sightly increasing costs, and reaches the minimum ($G/G_0 = \check{G}/G_0 = 0.79$) along a final branch that recovers the low cost of the initial solution.

For $N = 2$, both GBO paths continuously tend to $G/G_0 = 0.8$ isocontour by a significant increase of both performance and cost. In other words, the last GBO evaluations and two minima share almost constant values of G/G_0, but differ in both performance and cost ($p/p_0 \approx 1.1$; $c/c_0 \approx 0.85$ and $p/p_0 \approx 0.97$; $c/c_0 \approx 0.8$, for first and second run, respectively). GAO starts from dispersed individuals of the 1st population, including a single one lying in the sample cloud corresponding to thicker steel plate. Overall, the next populations develops with the same trend of the GBO runs. The last population has nearly the same G values

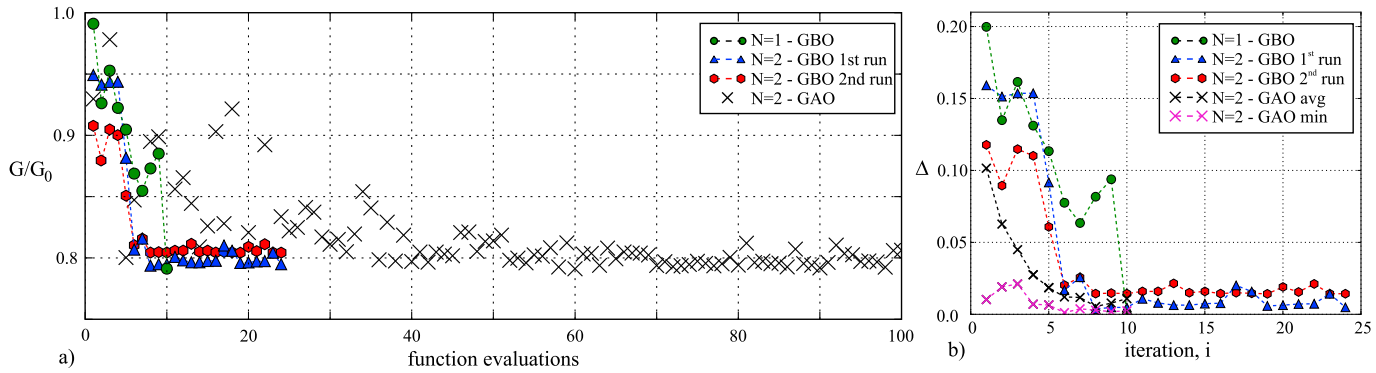

Fig. 17. GBO and GAO objective function for each function evaluation (a) and estimated error (b).

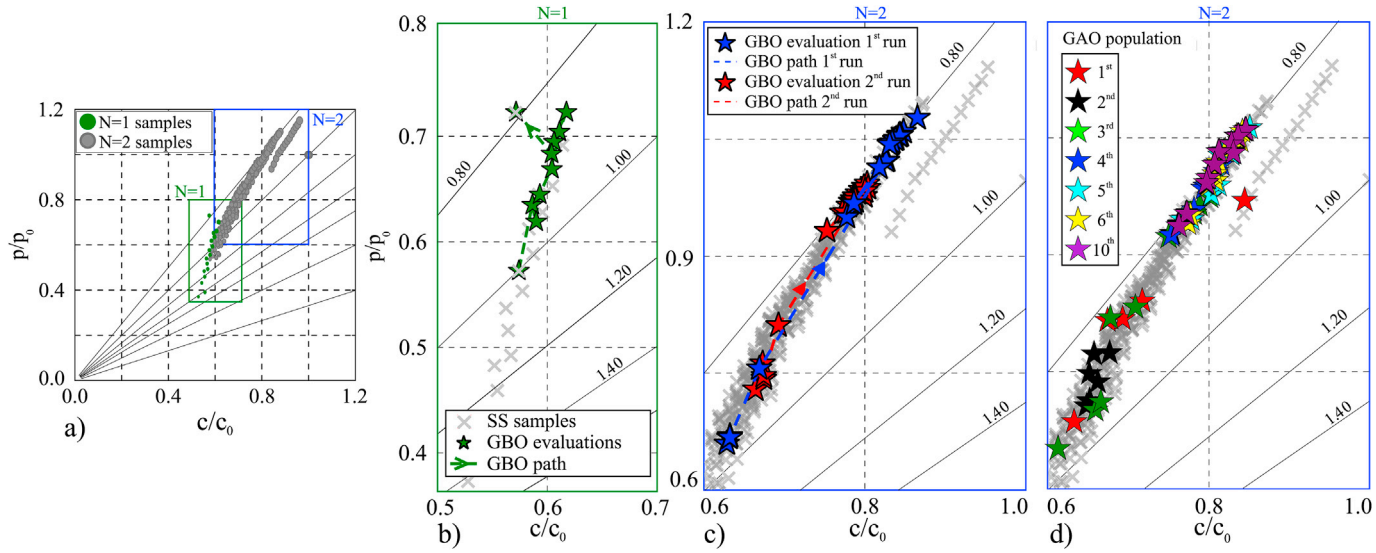

Fig. 18. Summary of the samples from the sensitivity study (SS) on the $c/c_0 - p/p_0$ plane (a), GBO and GAO paths for $N = 1$ (b) and $N = 2$ (c,d).

($G/G_0 \approx [0.79, 0.81]$), but significant differences in cost ($c/c_0 \approx [0.78, 0.85]$) and performance ($p/p_0 \approx [0.95, 1.06]$). Such differences in cost and performance for nearly equal G reflect the intrinsic multi-objective nature of the problem, and translate in different nearly-optimal shapes of the barrier.

Fig. 19 depicts optimal shapes from GBO and GAO for $N = 1$ and $N = 2$, to make comparisons between those and with the baseline shape. The GBO optimal shapes correspond to the design parameters minimizing G/G_0 (Fig. 19a). The GAO optimal shape corresponds to the individual of the last population that minimizes G/G_0. Nearly optimal shapes in the same population maximizing p/p_0, and minimizing c/c_0 are also plotted in Fig. 19(b). Overall, all optimal shapes have a higher vertical wall with respect to the baseline solution. The shape for $N = 1$ has the shortest overall curvilinear length, and his deflector curvature is close to the maximum one of the baseline solution. For N = 2 the GBO runs result in very similar optimal shapes ($s_1/H = 0.400$, $s_2/H = 0.438$, $h/H = 0.65$), and ($s_1/H = 0.455$, $s_2/H = 0.479$, $h/H = 0.633$), having deflector curvature higher than in the baseline solution. Conversely, GAO results in three distinct shapes, where: i. the optimal shape ($s_1/H = 0.411$, $s_2/H = 0.502$, $h/H = 0.65$) is close to the GBO optimal shapes; ii. the one corresponding to maximum performance ($s_1/H = 0.459$, $s_2/H = 0.514$, $h/H = 0.65$) is close to the optimal one, but has the largest curvilinear length; iii. the one corresponding to minimum cost ($s_1/H = 0.407$, $s_2/H = 0.506$, $h/H = 0.513$) is the closest to the baseline shape, even if its maximum deflector curvature is higher.

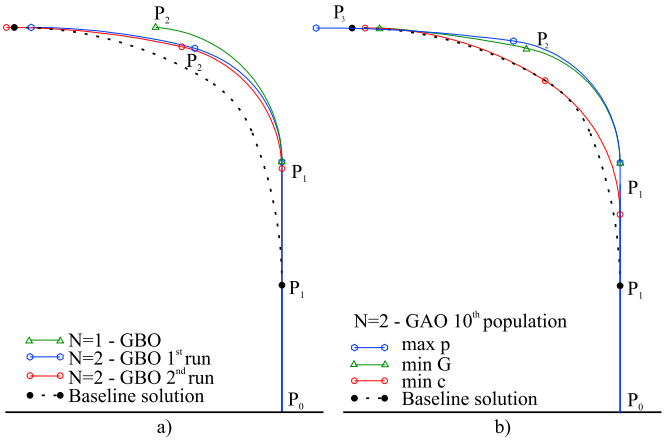

Fig. 19. Optimal shapes from GBO (a) and GAO (b).

7. Conclusion

The present study applies and discusses aerodynamic shape optimization to windblown sand barriers in turbulent atmospheric boundary layer. One specific barrier and two initial design solutions for its aerodynamic deflector are considered. For each of them, the optimization is carried out in the wake of extensive sensitivity studies, aimed at understanding the aerodynamic response of the barrier, at discussing the trend

of the objective function, and at selecting the optimization algorithm most suited to the specific case study. Optimization is carried out without recourse to surrogate models, and the evaluations of the goal function are obtained by Computational Fluid Dynamics simulations. Intensive computational campaign follows, including more than 600 computational simulations of the turbulent wind flow.

One-panel deflector is efficiently optimized by the gradient-based approach. The optimal solution dramatically reduces construction costs, but does not improve the performances of the baseline solution. Conversely, the optimization of two-panel deflector allows to both reduce construction costs and increase performances of the baseline barrier. In this case, a number of solutions obtained by genetic algorithm approach are nearly equivalent in terms of goal function minimum value. The choice of the final solution among them remains in charge of the designer, in the light of the specific needs of each project. The method applied and the lesson learned within the present study can be adopted to other applications belonging to the same class of problem, i.e. sand sedimentation around high-degree-of-bluffness barriers, where abrupt changes in their aerodynamic regime do not take place within the design space. For instance, most of the solid SMM barriers reviewed in Bruno et al. (2018c) belong to such a class of problems.

In the perspective of further optimization studies, a more general goal function can be expressed as c^n/p^m, where $n \neq m$. Such a definition allows to give different relative importance to both cost and performance. Due to the fact that both cost and performance are smooth functions of design variables, the presented optimization algorithm is able to work with the general form of the goal function above. In the perspective detailed design stage, the structural verification of the selected final solution shall be carried out on the basis of the wind-induced loads obtained by high-fidelity computational models (e.g. LES-based CFD simulations) and/or wind tunnel tests. Analogously, the detailed assessment of the sand trapping performances of the selected optimized barrier shall be assessed by means of full scale field tests in windy and sandy environments, or by scaled wind tunnel tests with incoming drifting sand, or by CFD simulations accounting for the multiphase modelling of windblown sand erosion, transport, and sedimentation.

Acknowledgments

The study has been developed in the framework of the MSCA-ITN-2016-EID research project Sand Mitigation around Railway Tracks (SMaRT, www.smart-eid.eu). The SMaRT project has received funding from the European Union Horizon 2020 research and innovation program under grant agreement No 721798. The authors wish to thank the other researchers of the SMaRT consortium for the helpful discussions about the topics of the paper. In particular the authors warmly thank L. Preziosi and D. Fransos, co-inventor of the S4S barrier, for the helpful discussions about the topics of the paper. Computational resources were provided by Optiflow Company and by HPC@POLITO, a project of Academic Computing within the Department of Control and Computer Engineering at the Politecnico di Torino (http://www.hpc.polito.it). The S4S patent is funded and managed by the Technology Transfer and Industrial Liaison Department of Politecnico di Torino.

References

Adams, B.M., Ebeida, M.S., Eldred, M.S., Geraci, G., Jakeman, J.D., Maupin, K.A., Monschke, J.A., Stephens, J.A., Swiler, L.P., Vigil, D.M., Wildey, T.M., 2014. Dakota, A multilevel parallel object-oriented framework for design optimization, parameter estimation, uncertainty quantification, and sensitivity analysis: version 6.9 user's manual. Optimization and uncertainty quantification department. URL: https://dakota.sandia.gov/sites/default/files/docs/6.9/Users-6.9.0.pdf. updated: November 13, 2018.

Alghamdi, A.A., Al-Kahtani, N.S., 2005. Sand control measures and sand drift fences. J. Perform. Constr. Facil. 19, 295–299. https://doi.org/10.1061/(ASCE)0887-3828(2005)19:4(295).

Araújo, A.D., Parteli, E.J.R., Pöschel, T., Andrade, J.S., Herrmann, H.J., 2013. Numerical modeling of the wind flow over a transverse dune. Nat. Sci. Rep. 3 https://doi.org/10.1038/srep02858.

Asghari Mooneghi, M., Kargarmoakhar, R., 2016. Aerodynamic mitigation and shape optimization of buildings: Review. J. Build. Eng. 6, 225–235. https://doi.org/10.1016/j.jobe.2016.01.009.

Bagnold, R., 1941. The Physics of Blown Sand and Desert Dunes. Methuen. https://doi.org/10.1007/978-94-009-5682-7.

Bagnold, R.A., 1936. The movement of desert sand. Proc. R. Soc. A Math. Phys. Eng. Sci. 157, 594. https://doi.org/10.1098/rspa.1936.0218.

Bagnold, R.A., 1937. The transport of sand by wind. Geogr. J. 89, 409–438. https://doi.org/10.2307/1786411.

Bernardini, E., Spence, S.M., Wei, D., Kareem, A., 2015. Aerodynamic shape optimization of civil structures: a cfd-enabled kriging-based approach. J. Wind Eng. Ind. Aerodyn. 144, 154–164. https://doi.org/10.1016/j.jweia.2015.03.011.

Bobby, S., Spence, S., Bernardini, E., Wei, D., Kareem, A., 2013. A complete performance-based optimization framework for the design of tall buildings. In: 11th International Conference on Structural Safety & Reliability. New York, NY, USA, 2013.

Bofah, K.K., Al-Hinai, K.G., 1986. Field tests of porous fences in the regime of sand-laden wind. J. Wind Eng. Ind. Aerodyn. 23, 309–319. https://doi.org/10.1016/0167-6105(86)90051-6.

Boyd, S., Vandenberghe, L., 2004. Convex Optimization. Cambridge University Press. URL: http://stanford.edu/~boyd/cvxbook/bv_cvxbook.pdf.

Bruno, L., Coste, N., Fransos, D., Lo Giudice, A., Preziosi, L., Raffaele, L., 2018a. Shield for sand: an innovative barrier for windblown sand mitigation. Recent Pat. Eng. 12, 237–246. https://doi.org/10.2174/1872212112666180309151818.

Bruno, L., Fransos, D., 2015. Sand transverse dune aerodynamic: 3d coherent flow structures from a computational study. J. Wind Eng. Ind. Aerodyn. 147, 291–301. https://doi.org/10.1016/j.jweia.2015.07.014.

Bruno, L., Fransos, D., Lo Giudice, A., 2018b. Solid barriers for windblown sand mitigation: aerodynamic behavior and conceptual design guidelines. J. Wind Eng. Ind. Aerodyn. 173, 79–90. https://doi.org/10.1016/j.jweia.2017.12.005.

Bruno, L., Horvat, M., Raffaele, L., 2018c. Windblown sand along railway infrastructures: a review of challenges and mitigation measures. J. Wind Eng. Ind. Aerodyn. 177, 340–365. https://doi.org/10.1016/j.jweia.2018.04.021.

Bruno, L., Preziosi, L., Fransos, D., 2016. A Deflecting Module for an Anti-sand Barrier, a Barrier Thus Obtained and a Protection Method from Windblown Sand. WO 2016/181417 A1.

Bruno, L., Salvetti, M., Ricciardelli, F., 2014. Benchmark on the aerodynamics of a rectangular 5:1 cylinder: an overview after the first four years of activity. J. Wind Eng. Ind. Aerodyn. 126, 87–106. https://doi.org/10.1016/j.jweia.2014.01.005.

Burman, J., Papila, N., Shyy, W., Gebart, B., 2002. Assessment of response surface-based optimization techniques for unsteady flow around bluff bodies. In: 9th AIAA/ISS- MO Symposium on Multidisciplinary Analysis and Optimization. Atlanta, Georgia. https://doi.org/10.2514/6.2002-5596.

Chepil, W., 1945. Dynamics of wind erosion: ii. initiation of soil movement. Soil Sci. 60, 397–411. https://doi.org/10.1097/00010694-194511000-00005.

Cid Montoya, M., Hernandez, S., Nieto, F., 2018a. Shape optimization of streamlined decks of cable-stayed bridges considering aeroelastic and structural constraints. J. Wind Eng. Ind. Aerodyn. 177, 429–455. https://doi.org/10.1016/j.jweia.2017.12.018.

Cid Montoya, M., Nieto, F., Hernandez, S., Kusano, I., Alvarez, A., Jurado, J., 2018b. Cfd-based aeroelastic characterization of streamlined bridge deck cross-sections subject to shape modifications using surrogate models. J. Wind Eng. Ind. Aerodyn. 177, 405–428. https://doi.org/10.1016/j.jweia.2018.01.014.

Ding, F., Kareem, A., 2018. A multi-fidelity shape optimization via surrogate modeling for civil structures. J. Wind Eng. Ind. Aerodyn. 178, 49–56. https://doi.org/10.1016/j.jweia.2018.04.022.

Dumas, L., 2008. CFD-based Optimization in Automotive Aerodynamics, Optimization and Computational Fluid Dynamics. Springer. https://doi.org/10.1007/978-3-540-72153-6_7.

Elshaer, A., Bitsuamlak, G., Damatty, A., 2015. Aerodynamic shape optimization for corners of tall buildings using cfd. In: 14th International Conference on Wind Engineering (ICWE). Porto Alegre, Brazil.

Elshaer, A., Bitsuamlak, G., El Damatty, A., 2017. Enhancing wind performance of tall buildings using corner aerodynamic optimization. Eng. Struct. 136, 133–148. https://doi.org/10.1016/j.engstruct.2017.01.019.

EN 1991-1-4, 2005. Eurocode 1: Actions on structures - part 1-4: General actions - wind actions - en 1991-1-4.

Forrester, A., Keane, A., 2009. Recent advances in surrogate-based optimization. Prog. Aerosp. Sci. 45, 50–79. https://doi.org/10.1016/j.paerosci.2008.11.001.

Gosselin, L., Tye-Gingras, M., Mathieu-Potvin, F., 2009. Review of utilization of genetic algorithms in heat transfer problems. Int. J. Heat Mass Transf. 52, 2169–2188. https://doi.org/10.1016/j.ijheatmasstransfer.2008.11.015.

Henry, J.C., 1952. American railroad on the arabian desert. Popul. Mech. 97, 107–110. URL: https://books.google.fr/books?id=ytwDAAAAMBAJ.

Hicks, R., Murman, E., Vanderplaats, G., 1974. An Assessment of Airfoil Design by Numerical Optimization. NASA Ames Research Center; Moffett Field, CA, United States. Technical Report. https://ntrs.nasa.gov/search.jsp?R=19740020369.

Karthik, K., Vishnu, M., Vengadesan, S., Bhattacharyya, S., 2018. Optimization of bluff bodies for aerodynamic drag and sound reduction using cfd analysis. J. Wind Eng. Ind. Aerodyn. 174, 133–140. https://doi.org/10.1016/j.jweia.2017.12.029.

Kawamura, R., 1951. Study of Sand Movement by Wind. NASA technical translation. Technical Report. https://archive.org/details/nasa_techdoc_19720013709.

Kerr, R., Nigra, J.O., 1952. Eolian sand control. Bull. Am. Assoc. Pet. Geol. 36, 1541–1573. https://doi.org/10.1306/5CEADB42-16BB-11D7-8645000102C1865D.

Li, B., Sherman, D.J., 2015. Aerodynamics and morphodynamics of sand fences: a review. Aeolian Res. 17, 33–48. https://doi.org/10.1016/j.aeolia.2014.11.005.

Li, Z., Zheng, X., 2017. Review of design optimization methods for turbomachinery aerodynamics. Prog. Aerosp. Sci. 93, 1–23. https://doi.org/10.1016/j.paerosci.2017.05.003.
Lima, I., Araújo, A., Parteli, E.J.R., Herrmann, H.J., 2017. Optimal array of sand fences. Sci. Rep. 7 https://doi.org/10.1038/srep45148.
Liu, B., Qu, J., Zhang, W., Qian, G., 2011. Numerical simulation of wind flow over transverse and pyramid dunes. J. Wind Eng. Ind. Aerodyn. 99, 879. https://doi.org/10.1016/j.jweia.2011.06.007.
Lo Giudice, A., Giammanco, G., Fransos, D., Preziosi, L., 2018. Modelling sand slides by a mechanics-based degenerate parabolic equation. Math. Mech. Solids. https://doi.org/10.1177/1081286518755230.
Mack, Y., Goel, T., Shyy, W., Haftka, R., 2005. Multiple surrogates for the shape optimization of bluff body-facilitated mixing. In: 43rd AIAA Aerospace Sciences Meeting and Exhibit. Reno, Nevada. https://doi.org/10.2514/6.2005-333.
Menter, F.R., 1994. Two-equation eddy-viscosity turbulence models for engineering applications. AIAA J. 32, 269–289. https://doi.org/10.2514/3.12149.
Menter, F.R., Kuntz, M., Langtry, R., 2003. Ten years of industrial experience with the SST turbulence model. In: Hanjalić, K., Nagano, Y., Tummers, J. (Eds.), Turbulence Heat and Mass Transfer 4: Proceedings of the Fourth International Symposium on Turbulence, Heat and Mass Transfer, Antalya, Turkey, 12-17 October, 2003. Begell House, p. 1208. URL: http://citeseerx.ist.psu.edu/viewdoc/download?doi=10.1.1.460.2814&rep=rep1&type=pdf.
Middleton, N., Sternberg, T., 2013. Climate hazards in drylands: a review. Earth Sci. Rev. 126, 48–57. https://doi.org/10.1016/j.earscirev.2013.07.008.
Mitchell, D.J., Fearnehough, W., Fullen, M.A., Trueman, I.C., 1996. Wind erosion and dune stabilisation in ningxia. China URL: http://www.uft.uni-bremen.de/Revitalisierung/texte/1996%20mitchell%20china%20sand%20stabil.pdf.
Munoz-Paniagua, J., Garcia, J., 2019. Aerodynamic surrogate-based optimization of the nose shape of a high-speed train for crosswind and passing-by scenarios. J. Wind Eng. Ind. Aerodyn. 184, 139–152. https://doi.org/10.1016/j.jweia.2018.11.014.
O'Brien, M., Rindlaub, B., 1936. The transportation of sand by wind. Civ. Eng. 6, 325–327.
Ooka, R., Chen, H., Kato, S., 2008. Study on optimum arrangement of trees for design of pleasant outdoor environment using multi-objective genetic algorithm and coupled simulation of convection, radiation and conduction. J. Wind Eng. Ind. Aerodyn. 96, 1733–1748. https://doi.org/10.1016/j.jweia.2008.02.039.
Pettus Newell, J., 1903. Sand Guards for Railroad Tracks, p. US731320.
Preziosi, L., Fransos, D., Bruno, L., 2015. A multiphase first order model for non-equilibrium sand erosion, transport and sedimentation. Appl. Math. Lett. 45, 69–75. https://doi.org/10.1016/j.aml.2015.01.011.
Pye, K., Tsoar, H., 2009. Aeolian Sand and Sand Dunes. Springer. https://doi.org/10.1007/978-3-540-85910-9.
Queipo, N.V., Haftka, R.T., Shyy, W., Goel, T., Vaidyanathan, R., Kevin, T.P., 2005. Surrogate-based analysis and optimization. Prog. Aerosp. Sci. 41, 1–28. https://doi.org/10.1016/j.paerosci.2005.02.001.
Raffaele, L., Bruno, L., Pellerey, F., Preziosi, L., 2016. Windblown sand saltation: a statistical approach to fluid threshold shear velocity. Aeolian Res. 23, 79–91. https://doi.org/10.1016/j.aeolia.2016.10.002.
Rahim, M., 1945. Behaviour of drift sand and method of dealing with it. In: Pakistan Engineering Congress.
Redding, J.H., Lord, J.A., 1981. Designing for the effects of windblown sand along the new Jessah-Riyadh-Dammam expressway. In: Symposium on Geotechnical Problems in Saudi Arabia, pp. 363–395.
Richards, P., Norris, S., 2011. Appropriate boundary conditions for computational wind engineering models revisited. J. Wind Eng. Ind. Aerodyn. 99, 257–266. https://doi.org/10.1016/j.jweia.2010.12.008.
Rizvi, A., 1989. Planning responses to aeolian hazards in arid regions. J. King Saud Univ. Architect. Plan. 1, 59–74.
Shao, Y., 2008. Physics and Modelling of Wind Erosion. Springer. https://doi.org/10.1007/978-1-4020-8895-7.
Simon, D., 2013. Evolutionary Optimization Algorithms: Biological Inspired and Population-Based Approaches to Computer Intelligence. John Wiley & Sons, Ltd.
Skinner, S., Zare-Behtash, H., 2018. State-of-the-art in aerodynamic shape optimisation methods. Appl. Soft Comput. 62, 933–962. https://doi.org/10.1016/j.asoc.2017.09.030.
Sweby, P.K., 1984. High resolution schemes using flux limiters for hyperbolic conservation laws. SIAM J. Numer. Anal. 21, 995–1011. https://doi.org/10.1137/0721062.
Wang, X.M., Zhang, C.X., Hasi, E., Dong, Z.B., 2010. Has the Three Norths Forest Shelterbelt Program solved the desertification and dust storm problems in arid and semiarid China? J. Arid Environ. 74, 13–22. https://doi.org/10.1016/j.jaridenv.2009.08.001.
Xue, Y., Zhai, Z., Chen, Q., 2013. Inverse prediction and optimization of flow control conditions for confined spaces using a cfd-based genetic algorithm. Build. Environ. 77 https://doi.org/10.1016/j.buildenv.2013.02.017.
Zhang, C., Zou, X., Cheng, H., Yang, S., Pan, X., Liu, Y., Dong, G., 2007. Engineering measures to control windblown sand in shiquanhe town, tibet. J. Wind Eng. Ind. Aerodyn. 95, 53–70. https://doi.org/10.1016/j.jweia.2006.05.006.
Zheng, X., 2009. Mechanics Wind-Blown Sand Movements. Springer-Verlag. https://doi.org/10.1007/978-3-540-88254-1.